

Copyright  
by  
Ali Moinfar  
2009

**TIME-LAPSE VARIATIONS OF MULTI-COMPONENT  
ELECTRICAL RESISTIVITY MEASUREMENTS ACQUIRED IN  
HIGH-ANGLE WELLS**

**by**

**ALI MOINFAR, B.Sc.**

**THESIS**

Presented to the Faculty of the Graduate School of  
The University of Texas at Austin  
in Partial Fulfillment  
of the Requirements  
for the Degree of

**MASTER OF SCIENCE IN ENGINEERING**

**The University of Texas at Austin**

**August 2009**

**TIME-LAPSE VARIATIONS OF MULTI-COMPONENT  
ELECTRICAL RESISTIVITY MEASUREMENTS ACQUIRED IN  
HIGH-ANGLE WELLS**

**Approved by**

**Supervising Committee:**

---

**Carlos Torres-Verdín, Supervisor**

---

**Kamy Sepehrnoori, Reader**

## **Dedication**

To

my wife, Leila Moravvej Farshi

and my parents, Mohammad Moinfar and Shamsi Mirkhani

without whose support none of this would be possible

## **Acknowledgements**

I am extremely thankful to my supervisor, Dr. Carlos Torres-Verdín, for his supervision, support, and friendship during this research. I thank the fellow students in our research group, in particular Robert K. Mallan for his collaboration in the development of this scientific study. I am also thankful to my friends Abdolhamid Hadibeik, Amirreza Rahmani, Benjamin Braneff, Dr. David Wolf, Jorge Sanchez, Renzo Angeles Boza, and Rohollah Abdollah Pour for their assistance during the research. I am also grateful to Rey Casanova and Cheryl Kruize for their kind help in personal and university-related paperwork. Special appreciation goes to Dr. Kamy Sepehrnoori for reviewing this thesis.

Funding for the work reported in this thesis was provided by UT Austin's Research Consortium on Formation Evaluation, jointly sponsored by Aramco, Anadarko, Baker-Hughes, BG, BHP Billiton, BP, Chevron, ConocoPhillips, ENI, ExxonMobil, Halliburton, Hess, Marathon, Mexican Institute for Petroleum, Nexen, Petrobras, Schlumberger, Shell International E&P, StatoilHydro, TOTAL, and Weatherford.

August 2009

## **Abstract**

# **TIME-LAPSE VARIATIONS OF MULTI-COMPONENT ELECTRICAL RESISTIVITY MEASUREMENTS ACQUIRED IN HIGH-ANGLE WELLS**

Ali Moinfar, M.S.E

The University of Texas at Austin, 2009

Supervisor: Carlos Torres-Verdín

Measurements of electrical conductivity anisotropy are becoming increasingly popular in LWD and open-hole environments. At the same time, field experience indicates that invasion and time of logging can have a significant effect on multi-component induction measurements acquired in high-angle wells, specifically in the presence of highly permeable formations and large contrasts of fluid density and viscosity. Some efforts have been made to study these effects, but the actual spatial distribution of fluid saturation due to invasion has not been considered in previous works. We use a commercial multi-phase fluid-flow simulator to reproduce invasion behavior in high-angle wells. Simulations provide us with an environment to reliably examine time-lapse effects of different geometrical and petrophysical parameters on the ensuing spatial

distribution of fluid saturation. The study considers the effects of both water- and oil-base muds invading hydrocarbon-bearing formations.

Simulations show that gravity segregation causes off-centered and asymmetric spatial distributions of electrical resistivity in high-angle wells. Furthermore, no-flow boundary conditions at impermeable shale boundaries cause high local concentration of mud-filtrate. These effects can vary significantly with time. Depending on the time of measurement acquisition after the onset of invasion, three-dimensional (3D) effects originating from invasion can distort the matrix of multi-component measurements. Consequently, inversion techniques should not be used blindly to synthesize all the measurements in the estimation of anisotropic electrical conductivity. It is imperative that 3D effects be diagnosed and separated in the analysis prior to estimating electrical resistivity anisotropy parallel and perpendicular to bedding plane. We suggest that opposite signs of cross-coupled components as well as non-monotonic variations of coplanar components over time could be used to discern invasion effects from other 3D effects.

## Table of Contents

<b>Acknowledgments</b> .....	<b>v</b>
<b>Abstract</b> .....	<b>vi</b>
<b>Table of Contents</b> .....	<b>viii</b>
<b>List of Tables</b> .....	<b>x</b>
<b>List of Figures</b> .....	<b>xi</b>
<b>Chapter 1: Introduction</b> .....	<b>1</b>
<b>Chapter 2: Numerical Simulation of Mud-Filtrate Invasion</b> .....	<b>7</b>
2.1 Reservoir Model .....	7
2.2 Method .....	12
2.3 Simulation Results of WBM Invasion .....	13
2.4 Discussion .....	18
<b>Chapter 3: Simulation of Multi-Component Induction Measurements</b> .....	<b>19</b>
3.1 Method .....	19
3.2 Apparent Conductivity .....	20
3.3 Simulation Results .....	20
3.4 Pseudo Electrical Anisotropy.....	24
3.5 Time-Lapse Variation of Multi-Component Induction Measurements ..	29
3.6 Layer-Thickness Effects .....	33
3.7 Effect of Well-Deviation Angle.....	35
<b>Chapter 4: Oil-Base Mud-Filtrate Invasion</b> .....	<b>37</b>
4.1 Reservoir Model .....	37
4.2 Simulation Results of OBM Invasion .....	39
4.3 Simulation of Multi-Component Induction Measurements .....	41
<b>Chapter 5: Summary and Conclusions</b> .....	<b>44</b>
5.1 Summary .....	44
5.2 Conclusions .....	44

<b>References .....</b>	<b>47</b>
<b>Vita ..</b>	<b>50</b>

## List of Tables

<b>TABLE 2.1:</b> Summary of petrophysical and fluid properties assumed in the simulation of water-base mud-filtrate invasion.....	11
<b>TABLE 3.1:</b> Apparent horizontal and vertical conductivities simulated at different times after the onset of invasion in the vertical well. ....	32
<b>TABLE 3.2:</b> Apparent horizontal and vertical conductivities simulated at different times after the onset of invasion in the 70° well.....	32
<b>TABLE 4.1:</b> Summary of the properties of pseudo components assumed in the simulation of OBM invasion.....	39

## List of Figures

- Figure 1.1:** Schematic configuration of the assumed multi-component induction tool. The symbols  $T_x$ ,  $T_y$ , and  $T_z$  identify three collocated orthogonal transmitter coils and  $R_x$ ,  $R_y$ , and  $R_z$  identify three collocated orthogonal receiver coils. At each logging depth, the tool acquires a  $3 \times 3$  matrix of measurements.  $H_{pq}$  denotes the magnetic field measured by the  $q$ -oriented receiver and excited by the  $p$ -oriented transmitter. In this study we assume short and long transmitter-receiver spacings (offsets) of 0.4 m and 1.8 m, respectively. .... 2
- Figure 2.1:** Synthetic sand-shale laminated reservoir model constructed to appraise invasion effects on multi-component induction measurements. The thickness of sand layers ranges from 40-ft thick at the top to 1-ft thick at the bottom. All shale laminations are 1-ft thick. The reservoir is assumed shouldered by thick shale beds. ....8
- Figure 2.2:** Outcrop analogue of the synthetic reservoir model described in Figure 2.1 (turbidite sedimentary sequence in the Tanqua area, South Africa; photograph courtesy of Chris Lerch, BHP Billiton). ....9
- Figure 2.3:** Saturation-dependent (a) capillary pressure and (b) relative permeability assumed in the simulation of water-base mud-filtrate invasion. The symbol  $k_{rw}$  denotes the relative permeability of water which is the wetting phase and  $k_{ro}$  is that of oil which is the non-wetting phase. ....10

<b>Figure 2.4:</b> Cross-sections of the spatial distributions of (a) water saturation, (b) salt concentration, and (c) electrical conductivity after 2 days of WBM invasion in a vertical well. The first row shows the vertical cross-sections and the second row shows the cross-sections perpendicular to the borehole axis simulated in the center of the top layer.....	15
<b>Figure 2.5:</b> Spatial distributions of water saturation, salt concentration, and electrical resistivity resulting from the simulation of mud-filtrate invasion with WBM. Panel (a) shows the XZ cross-section of water saturation in the 10-ft layer. Panels (b), (c), and (d) show cross-sections of water saturation, salt concentration, and electrical conductivity, respectively, perpendicular to the borehole axis simulated in the center of the top layer. The first, second, and third rows correspond to $t=0.1$ , $t=0.5$ , and $t=2$ days of invasion, respectively. Relative dip is $70^\circ$ .....	16
<b>Figure 2.6:</b> Radial distributions of (a) water saturation and salt concentration, and (b) formation resistivity, simulated at $t=0.5$ and $t=2$ days of WBM-filtrate invasion.....	17
<b>Figure 3.1:</b> Comparison of (a) $\sigma_{zz}$ and (b) $\sigma_{xx}$ responses simulated before and after 2 days of WBM-filtrate invasion. Receiver offset is 0.4 m and operating frequency is 25 kHz. The well is vertical. ....	21
<b>Figure 3.2:</b> Comparison of (a) $\sigma_{zz}$ , (b) $\sigma_{xx}$ , (c) $\sigma_{yy}$ , (d) $\sigma_{zx}$ , and (e) $\sigma_{xz}$ responses simulated before and after 2 days of WBM-filtrate invasion. Receiver offset is 0.4 m and operating frequency is 25 kHz. Dip angle is $70^\circ$ . ....	22
<b>Figure 3.3:</b> Comparison of (a) $\sigma_{zz}$ , (b) $\sigma_{xx}$ , (c) $\sigma_{yy}$ , (d) $\sigma_{zx}$ , and (e) $\sigma_{xz}$ responses simulated before and after 2 days of WBM-filtrate invasion. Receiver offset is 1.8 m and operating frequency is 25 kHz. Dip angle is $70^\circ$ . ....	23

<b>Figure 3.4:</b> Direct-coupled components of apparent conductivity (XX, YY, and ZZ) simulated in both vertical and 70° wells (a) before WBM-filtrate invasion, and (b) after 2 days of invasion. Receiver offset is 0.4 m and operating frequency is 25 kHz. ....	27
<b>Figure 3.5:</b> Cross-coupled components of apparent conductivity (XZ, ZX) simulated in the 70° well compared before and after 2 days of WBM-filtrate invasion. Receiver offset is 0.4 m and operating frequency is 25 kHz.....	28
<b>Figure 3.6:</b> Comparison of (a) $\sigma_{zz}$ , (b) $\sigma_{xx}$ , (c) $\sigma_{yy}$ , and (d) $\sigma_{zx}$ responses simulated at different times of acquisition after the onset of WBM-filtrate invasion. Receiver offset is 0.4 m and operating frequency is 25 kHz. Dip angle is 70°.....	30
<b>Figure 3.7:</b> Comparison of (a) $\sigma_{xx}$ and (b) $\sigma_{yy}$ responses simulated at different times of acquisition after the onset of WBM-filtrate invasion. Receiver offset is 1.8 m and operating frequency is 25 kHz. Dip angle is 70°.....	31
<b>Figure 3.8:</b> Deviation of (a) $\sigma_{zz}$ , (b) $\sigma_{xx}$ , and (c) $\sigma_{yy}$ , responses from true layer conductivity simulated in the center of different layers as a function of their thicknesses before and after 2 days of WBM-filtrate invasion. ....	34
<b>Figure 3.9:</b> Comparison of (a) $\sigma_{zz}$ , (b) $\sigma_{xx}$ , (c) $\sigma_{yy}$ , (d) $\sigma_{zx}$ , and (e) $\sigma_{xz}$ responses after 2 days of WBM-filtrate invasion acquired at different angles of well deviation. Receiver offset is 0.4 m and operating frequency is 25 kHz. ....	35
<b>Figure 3.10:</b> Comparison of (a) $\sigma_{zz}$ and (b) $\sigma_{zx}$ responses at the top layer after 2 days of WBM-filtrate invasion acquired at different angles of well deviation. Receiver offset is 0.4 m and operating frequency is 25 kHz. ....	36

<b>Figure 4.1:</b> (a) Wetting-phase saturation-dependent capillary pressure assumed in the simulation of OBM- filtrate invasion, and (b) Corresponding saturation-height distribution showing the top and the bottom limits of the reservoir. ....	38
<b>Figure 4.2:</b> Cross-sections of the spatial distributions of (a) water saturation, and (b) electrical conductivity, perpendicular to the borehole, simulated after 0.1 days of OBM-filtrate invasion. The images intersect the center of the 4-ft thick layer in the model shown in Figure 2.1. Dip angle is 70°. ....	40
<b>Figure 4.3:</b> Comparison of (a) $\sigma_{zz}$ , (b) $\sigma_{xx}$ , (c) $\sigma_{yy}$ , (d) $\sigma_{zx}$ , and (e) $\sigma_{xz}$ responses simulated before and after 2 days of OBM-filtrate invasion. Receiver offset is 0.4 m and operating frequency is 25 kHz. Dip angle is 70°. ....	42
<b>Figure 4.4:</b> Comparison of (a) $\sigma_{zz}$ , and (b) $\sigma_{xx}$ responses simulated in a vertical well and a 70°-well before and after 2 days of OBM-filtrate invasion. Receiver offset is 0.4 m and operating frequency is 25 kHz. Dip angle is 70°. ....	43

# CHAPTER 1

## INTRODUCTION

Laminated sand-shale sequences in deepwater turbidite reservoirs hold a significant amount of the world's hydrocarbon reserves. Conventional resistivity measurements are not adequate for the petrophysical evaluation of thinly laminated sand-shale sequences. Thin hydrocarbon-bearing resistive sands that are adjacent to conductive shales are usually bypassed with conventional induction measurements. However, multi-component induction tools are now commercially available that provide the additional measurements necessary to accurately characterize the properties of laminated sand-shale sequences. Inversion of multi-component induction measurements provides vertical resistivity in addition to horizontal resistivity measured by conventional tools. Therefore, multi-component measurements are sensitive to resistivity anisotropy.

Figure 1.1 shows the schematic configuration of a multi-component induction tool. This tool consists of three collocated orthogonal transmitter coils ( $T_x$ ,  $T_y$ ,  $T_z$ ) and three collocated orthogonal receiver coils ( $R_x$ ,  $R_y$ ,  $R_z$ ). The instrument acquires nine components of the magnetic field at every logging depth: the co-axial direct-coupled component  $H_{zz}$ , transverse or co-planar direct-coupled components  $H_{xx}$  and  $H_{yy}$ , and cross-coupled components  $H_{xy}$ ,  $H_{yx}$ ,  $H_{yz}$ ,  $H_{zy}$ ,  $H_{xz}$ , and  $H_{zx}$ , where  $H_{pq}$  denotes the magnetic field measured by a q-oriented receiver and excited by the p-oriented transmitter. Conventional induction tools measure only the co-axial component. The  $3 \times 3$

matrix of multi-component induction measurements is sensitive, among other factors, to formation electrical anisotropy and relative dip. Thus, these latter conditions can be inferred from the measurements with advanced inversion techniques.

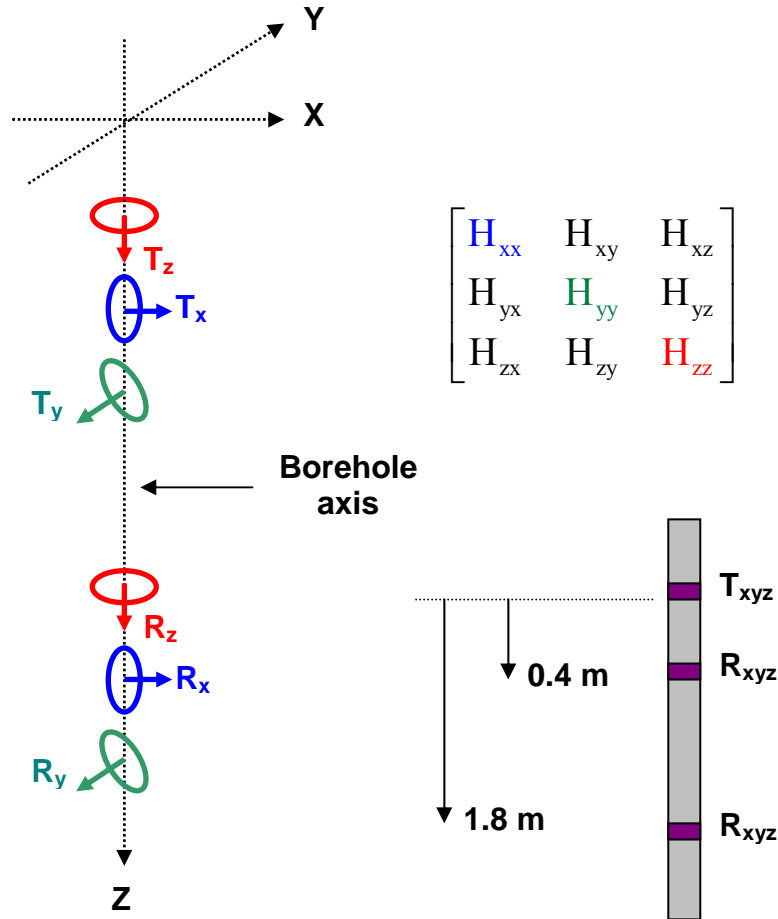


**Figure 1.1:** Schematic configuration of the assumed multi-component induction tool. The symbols  $T_x$ ,  $T_y$ , and  $T_z$  identify three collocated orthogonal transmitter coils and  $R_x$ ,  $R_y$ , and  $R_z$  identify three collocated orthogonal receiver coils. At each logging depth, the tool acquires a 3x3 matrix of measurements.  $H_{pq}$  denotes the magnetic field measured by the q-oriented receiver and excited by the p-oriented transmitter. In this study we assume short and long transmitter-receiver spacings (offsets) of 0.4 m and 1.8 m, respectively.

Resistivity anisotropy is a typical characteristic of laminated sand-shale formations. Large resistivity anisotropy observed in these formations is the result of the resistivity contrast between resistive hydrocarbon-bearing sands and conductive water-bearing shales. Therefore, petrophysical evaluation of these formations is mainly based on detecting electrical resistivity anisotropy. Several interpretation techniques have been developed in the last decade to determine vertical and horizontal resistivities from multi-component induction measurements (Klein et al., 1997; Yu et al., 2001; Kreigshauser et al., 2001; Rabinovich and Tabarovsky, 2001; Zhang et al., 2001). Likewise, different resistivity anisotropy models have been proposed to calculate sand resistivity from vertical and horizontal resistivities (Mollison et al., 1999; Clavaud et al., 2005). Pure-sand resistivity in conjunction with other available logs and core data result in more reliable estimation of hydrocarbon reserves in thinly laminated sand-shale reservoirs. Several case studies have shown the added value of multi-component induction measurements in identifying additional hydrocarbon pay zones (Gomes et al., 2002; Saxena and Klimentos, 2004).

Alternating layers of sand and shale in thinly laminated formations is not the only cause of resistivity anisotropy. This type of anisotropy is usually referred to as macroscopic electrical anisotropy. Alternating thin sand layers with different resistivities can also create macroscopic anisotropy. However, there are other physical sources of electrical anisotropy. Shales often exhibit resistivity anisotropy originating from their micro-bedding structure. Clay minerals included in shale layers often exhibit growth and stacking patterns that produce intrinsic anisotropy. This kind of anisotropy is called

microscopic anisotropy. The microscopic dimension is much smaller than measurement resolution while the macroscopic size is of the order of the measurement resolution.

True electrical anisotropy gives rise to symmetric off-diagonal entries in the matrix of magnetic multi-component measurements (Omeragic et al., 2006). However, 3D effects can also give rise to off-diagonal components of the matrix of magnetic multi-components. When not properly diagnosed, such effects can cause false estimations of intrinsic electrical anisotropy. That is, the formation under consideration is not intrinsically anisotropic, but induction logging measurements exhibit behavior similar to that due to electrical anisotropy. A bed terminating near the borehole or a fault intersecting with the wellbore are examples of 3D measurement effects. Henceforth we refer to these generic 3D measurement effects as pseudo electrical anisotropy effects.

In this study, we study another possible 3D effect on multi-component induction measurements which can be a source of pseudo electrical anisotropy. Invasion of mud-filtrate into porous and permeable layers may lead to pseudo electrical anisotropy because of the resulting non-uniform spatial distribution of electrical resistivity near the borehole region. More importantly, because the process of invasion is dynamic, this distribution changes over time and therefore, the matrix of measurements becomes time dependent. In this study we focus on mud-filtrate invasion as the only possible cause of time-lapse pseudo electrical anisotropy. Consequently, it is important to consider the effects of mud-filtrate invasion to accurately infer vertical and horizontal resistivities from multi-component induction measurements. Pseudo electrical anisotropy can result in biased

calculations of pure-sand resistivity, thereby in biased estimations of fluid saturation. We emphasize that multi-component induction measurements should not be blindly inverted to compute vertical and horizontal resistivities. It is necessary to separate true anisotropy due to sand-shale laminations and pseudo anisotropy originating from asymmetric invasion to avoid false petrophysical interpretations of thinly laminated sand-shale reservoirs. This problem can be of great importance in the evaluation of deepwater formations where exploration and development costs are extremely high.

A few studies have been performed to investigate the effects of invasion on multi-component induction measurements. Barber et al. (2004) found that their successfully-tested processing method for calculating formation resistivity anisotropy was not adequate to determine anisotropy in zones invaded with conductive mud. Mallan and Torres-Verdín (2006) examined the sensitivity of different induction components to radial length of invasion in a deviated well environment. Both studies assumed a parametric and piston-like invasion model around the borehole with a step conductivity profile. However, this assumption is not realistic, especially in highly deviated wells where gravity segregation causes off-centered and asymmetric spatial distributions of mud filtrate near the borehole region. Wu et al. (2001) examined the sensitivity of the co-axial induction response to numerically simulated mud-filtrate invasion in a vertical well. Furthermore, Alpak et al. (2003) and Mallan and Torres-Verdín (2006) described the effects of numerically simulated water-base mud-filtrate invasion in a horizontal well on co-axial and multi-component induction measurements, respectively.

In this study, we investigate the effects of numerically simulated mud-filtrate invasion on multi-component induction measurements acquired in vertical and high-angle wells. We consider the effects of both water-base mud (WBM) and oil-base mud (OBM) invading hydrocarbon-bearing formations. Comparisons are made of the spatial distribution of invasion in vertical and high-angle wells to show that the matrix of multi-component induction measurements is non-diagonal for the case of invasion in a high-angle well. Moreover, we describe cases of time-lapse pseudo electrical anisotropy originating from mud-filtrate invasion in vertical and high-angle wells. We also describe some specific effects of mud-filtrate invasion on multi-component measurements that can be a great help in distinguishing invasion effects from other 3D measurement effects.

## CHAPTER 2

### NUMERICAL SIMULATION OF MUD-FILTRATE INVASION

This chapter describes the formation model considered for the simulation of water-base mud-filtrate invasion. We also implement a 3D numerical method to simulate the process of mud-filtrate invasion acquired in high-angle wells. Subsequently, we describe spatial distributions of water saturation, salt concentration, and electrical conductivity resulting from the simulation of mud-filtrate invasion.

#### 2.1 RESERVOIR MODEL

Numerical simulation of mud-filtrate invasion and multi-component induction measurements are performed across the reservoir model shown in Figure 2.1. This layered model comprises a set of resistive sand layers with thicknesses ranging from 40-ft to 1-ft, which are hydraulically isolated from each other by thin conductive shale beds. The synthetic model is representative of a deepwater turbidite reservoir similar to the outcrop shown in Figure 2.2. We first illustrate our procedure for the case of WBM invasion and later we implement the method in the presence of OBM invasion. Table 2.1 summarizes the petrophysical and fluid parameters assumed in the simulation of WBM invasion. Figure 2.3 describes the assumed saturation-dependant capillary pressure and relative permeability. For the case of WBM, we assume that all sands are initially saturated with oil up to the level of irreducible water saturation.

We perform our simulations for the cases of a vertical well and a high-angle well with relative dip of  $70^\circ$ . Due to memory constraints, we simulate the invasion in each individual sand layer separately and then combine the individual simulations to construct the complete model. No limitation arises with this implementation since the sand layers do not exhibit cross flow due to presence of impermeable shale layers between them.

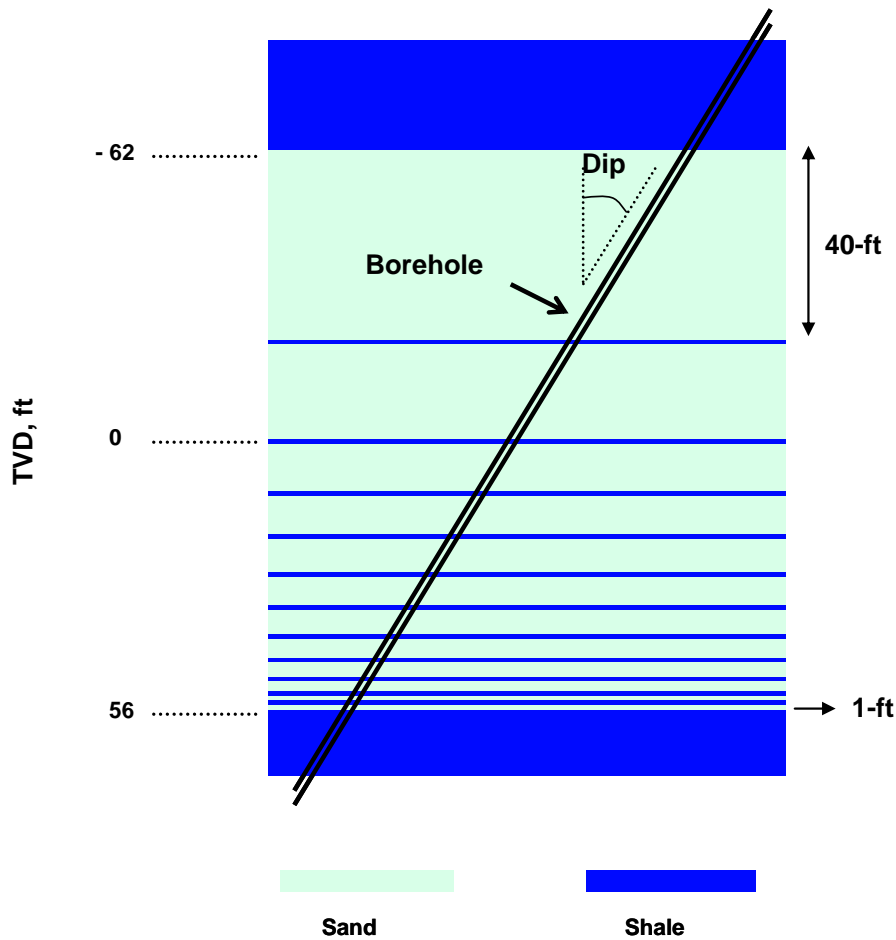


**Figure 2.1:** Synthetic sand-shale laminated reservoir model constructed to appraise invasion effects on multi-component induction measurements. The thickness of sand layers ranges from 40-ft thick at the top to 1-ft thick at the bottom. All shale laminations are 1-ft thick. The reservoir is assumed shouldered by thick shale beds.

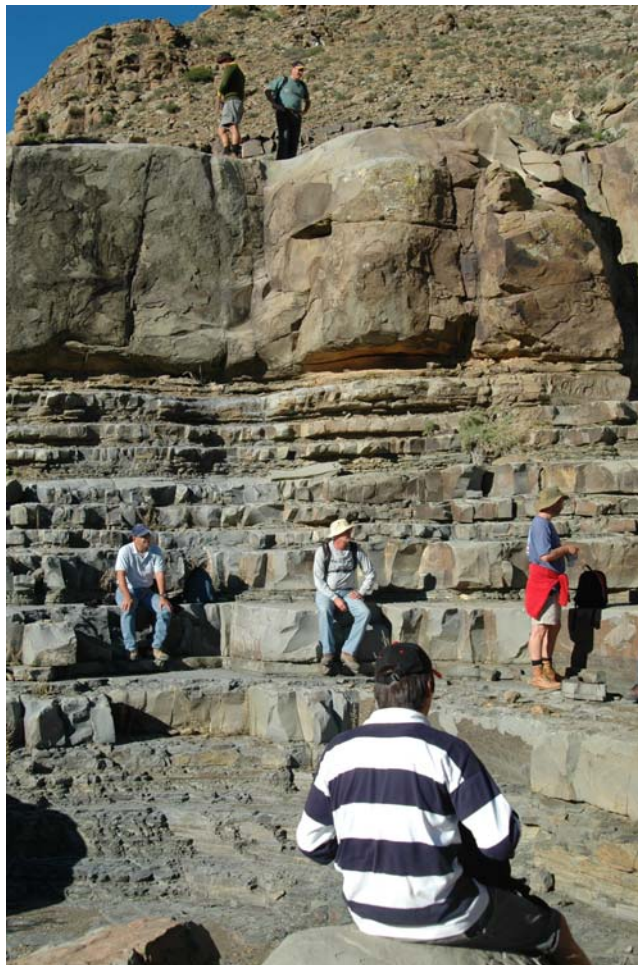


**Figure 2.2:** Outcrop analogue of the synthetic reservoir model described in Figure 2.1 (turbidite sedimentary sequence in the Tanqua area, South Africa; photograph courtesy of Chris Lerch, BHP Billiton).

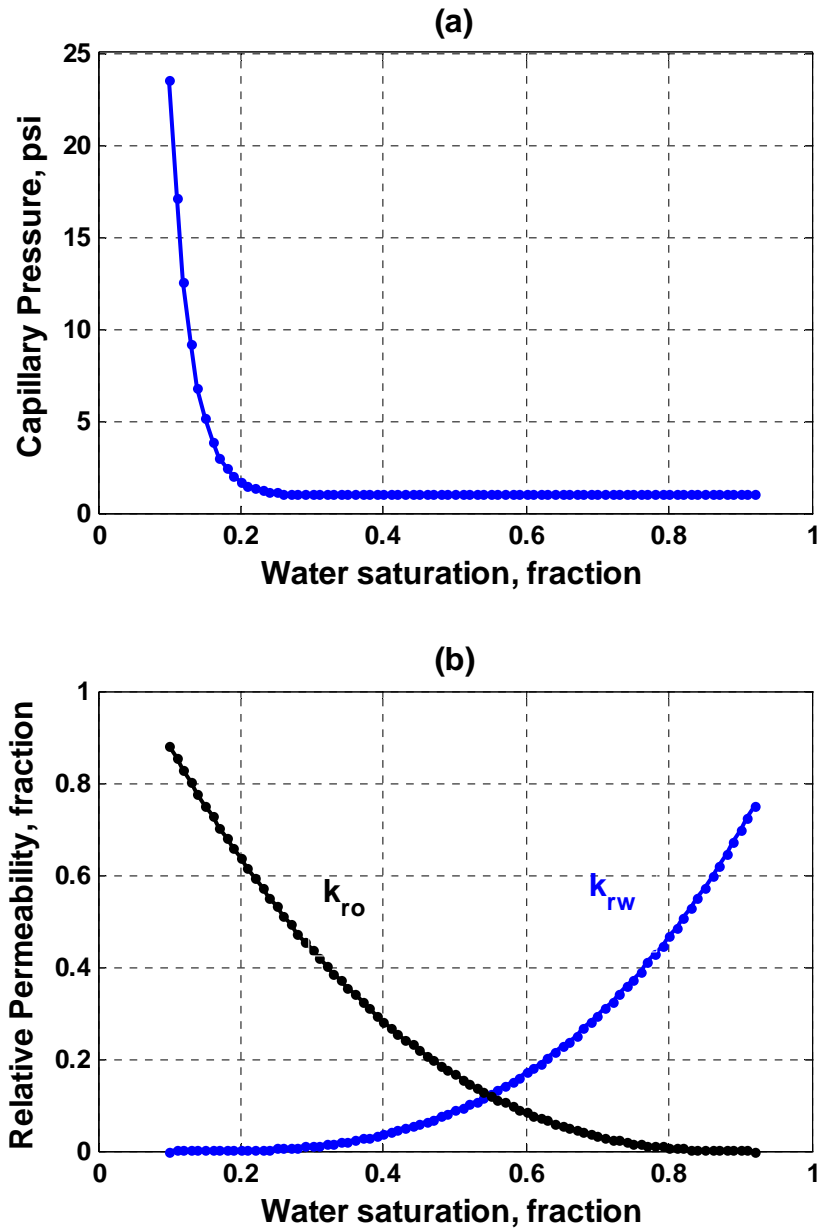


**Figure 2.3:** Saturation-dependent (a) capillary pressure and (b) relative permeability assumed in the simulation of water-base mud-filtrate invasion. The symbol  $k_{rw}$  denotes the relative permeability of water which is the wetting phase and  $k_{ro}$  is that of oil which is the non-wetting phase.

Variable	Units	Value
Sand porosity	fraction	0.28
Sand permeability	md	500
Shale porosity	fraction	0.12
Shale permeability	md	0
Irreducible water saturation	fraction	0.1
Residual oil saturation	fraction	0.08
Water density	gr/cm <sup>3</sup>	1.00
Oil density	gr/cm <sup>3</sup>	0.70
Water viscosity	cp	1
Oil viscosity	cp	0.5
Connate water salt concentration	ppm	180,000
Mud-filtrate salt concentration	ppm	10,000
Depth	ft	9100
Formation pressure	psi	3940
Formation temperature	°F	188
Wellbore diameter	in	8.5
Invasion rate	bbl/day/ft	0.24
Overbalance pressure	psi	500
Maximum invasion time	days	2
Shale electrical conductivity	S/m	1.0

**TABLE 2.1:** Summary of petrophysical and fluid properties assumed in the simulation of water-base mud-filtrate invasion.

## 2.2 METHOD

We use the compositional Computing Modeling Group's (CMG-STARs) fluid-flow simulator to reproduce the process of mud-filtrate invasion in porous and permeable sand layers. Simulations are performed with a 3D Cartesian grid with corner point geometry. In so doing, we discretize the wellbore into a sequence of finite-square grid blocks. This discretization strategy enables the accurate implementation of a deviated wellbore (Angeles, 2009). We place injectors around the surface of the wellbore and enforce injection boundary conditions equivalent to invasion at a constant rate. Numerical simulation generates values of water saturation and salt concentration at each grid node for different times of acquisition after the onset of invasion. Electrical conductivity of water is calculated at each grid node via the formula (Zhang et al., 1999):

$$\sigma_w = \left[ \left( 0.0123 + \frac{3647.5}{C_w^{0.995}} \right) \times \frac{81.77}{T + 6.77} \right]^{-1}, \quad (1)$$

where  $C_w$  is salt concentration in ppm,  $T$  is formation temperature in °F, and  $\sigma_w$  is electrical conductivity of formation connate water in S/m. We apply Archie's equation (Archie, 1942) to transform the spatial distribution of water saturation into the equivalent spatial distribution of formation conductivity, given by

$$\sigma_t = \sigma_w \left( \frac{\phi^m}{a} \right) S_w^n, \quad (2)$$

where  $\sigma_t$ ,  $\sigma_w$ ,  $\phi$ , and  $S_w$  denote formation conductivity, connate water conductivity, porosity, and water saturation, respectively, with the choice of constants  $a=1$ ,  $m=2$ , and  $n=2$ . The scalar electrical conductivity grid is mapped into a  $40 \times 40 \times 106$  Cartesian grid to accommodate the 3D multi-component finite-difference electromagnetic (EM) modeling code.

### 2.3 SIMULATION RESULTS OF WBM INVASION

We use the CMG-STARs simulator to reproduce the process of mud-filtrate invasion for both vertical and highly deviated wells drilled with WBM. While the spatial distribution of mud filtrate in vertical wells is axially symmetric around the wellbore, it has a more complex shape in high-angle wells that depends on time of logging. Figure 2.4 shows cross-sections of the spatial distributions of water saturation, salt concentration, and bulk electrical conductivity after 2 days of invasion in a vertical well. Figure 2.5 shows the same cross-sections after 0.1, 0.5, and 2 days of invasion in a  $70^\circ$  well. It is inferred from Figures 2.4 and 2.5 that gravity segregation causes an off-centered and asymmetric spatial distribution of mud filtrate in the  $70^\circ$  well. Figure 2.5 also compares cross-sections of the spatial distributions of water saturation, salt concentration, and bulk electrical conductivity at different times of acquisition after the onset of invasion, indicating that water-base mud-filtrate sags down around the borehole over time. Moreover, Figure 2.5a shows that the no-flow boundary condition at the impermeable shale boundary causes mud filtrate to concentrate at the bottom of the sand layer. The impact of bed boundary on the spatial distribution of mud-filtrate is included in the simulation of multi-component measurements. Figure 2.5a depicts the spatial

distribution of invasion only within a 10-ft layer. Remaining sand layers in the model are subjected to mud-filtrate invasion in a similar fashion.

As shown in Figure 2.5d, the spatial distribution of electrical conductivity is different on either side of the borehole. The resistive annulus observed above the borehole is a result of unstable displacement of mud-filtrate in the high-angle well. As time progresses, mud-filtrate does not invade further above the borehole and begins to sag down around it. Also, since WBM has a lower salt concentration than connate water, there is a continuous diffusion of salt in the opposite direction of mud-filtrate invasion due to salt mixing. Figure 2.6 shows radial profiles of water saturation, salt concentration, and electrical resistivity perpendicular to the borehole axis at two different times of acquisition after the onset of invasion. We infer that the salt concentration front leads the water saturation front above the borehole over time, thereby causing a resistive annulus to appear there. However, there is no resistive annulus below the borehole because the water saturation front does not lag the salt concentration front as a result of continuous downward invasion of mud-filtrate in that region.

With this strategy, the CMG fluid-flow simulator provides us with an environment to reliably examine the effects of different geometrical and petrophysical properties on mud-filtrate invasion and, therefore, on the spatial distribution of electrical conductivity around the borehole.

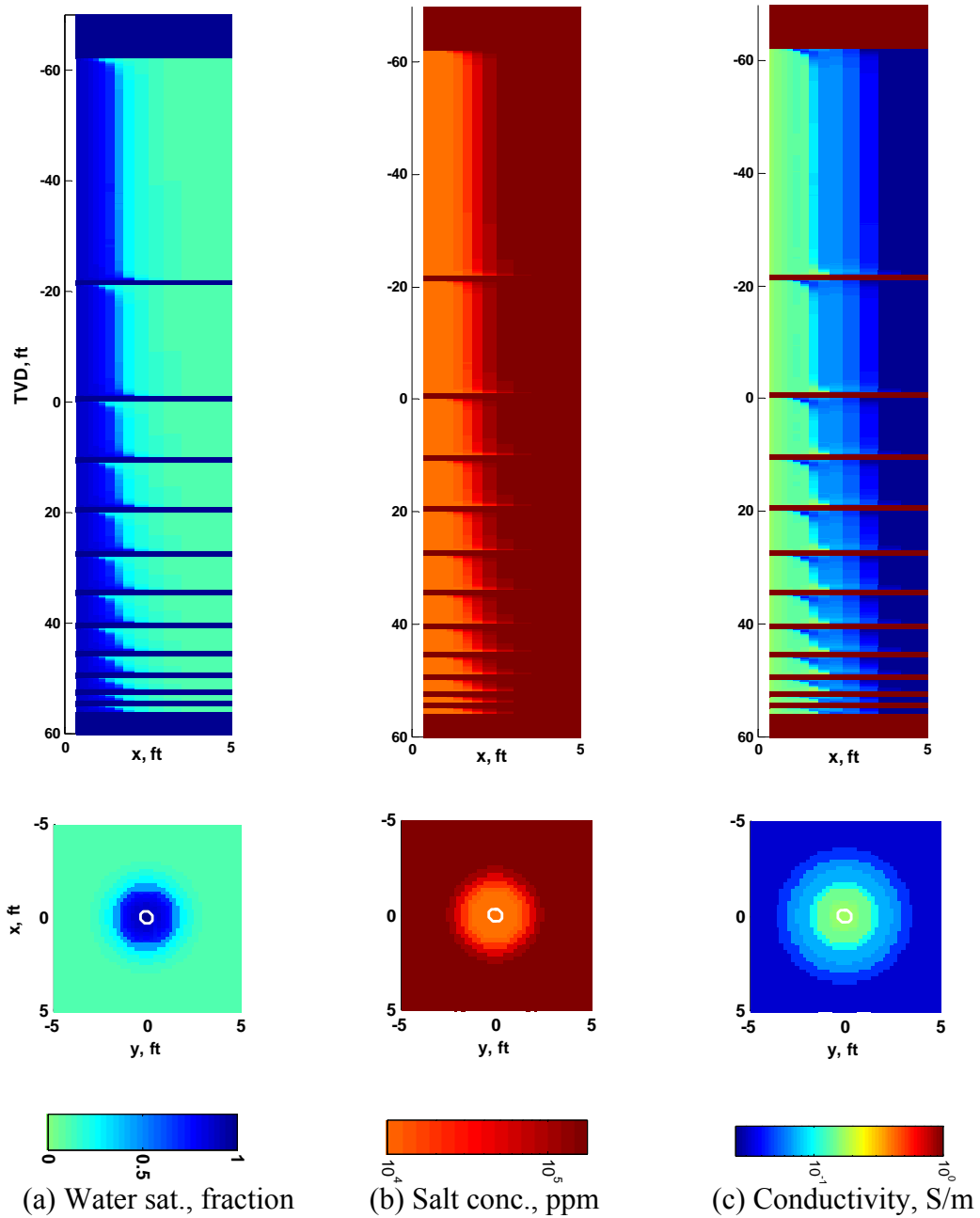


**Figure 2.4:** Cross-sections of the spatial distributions of (a) water saturation, (b) salt concentration, and (c) electrical conductivity after 2 days of WBM invasion in a vertical well. The first row shows vertical cross-sections whereas the second row shows cross-sections perpendicular to the borehole axis simulated in the center of the top layer.

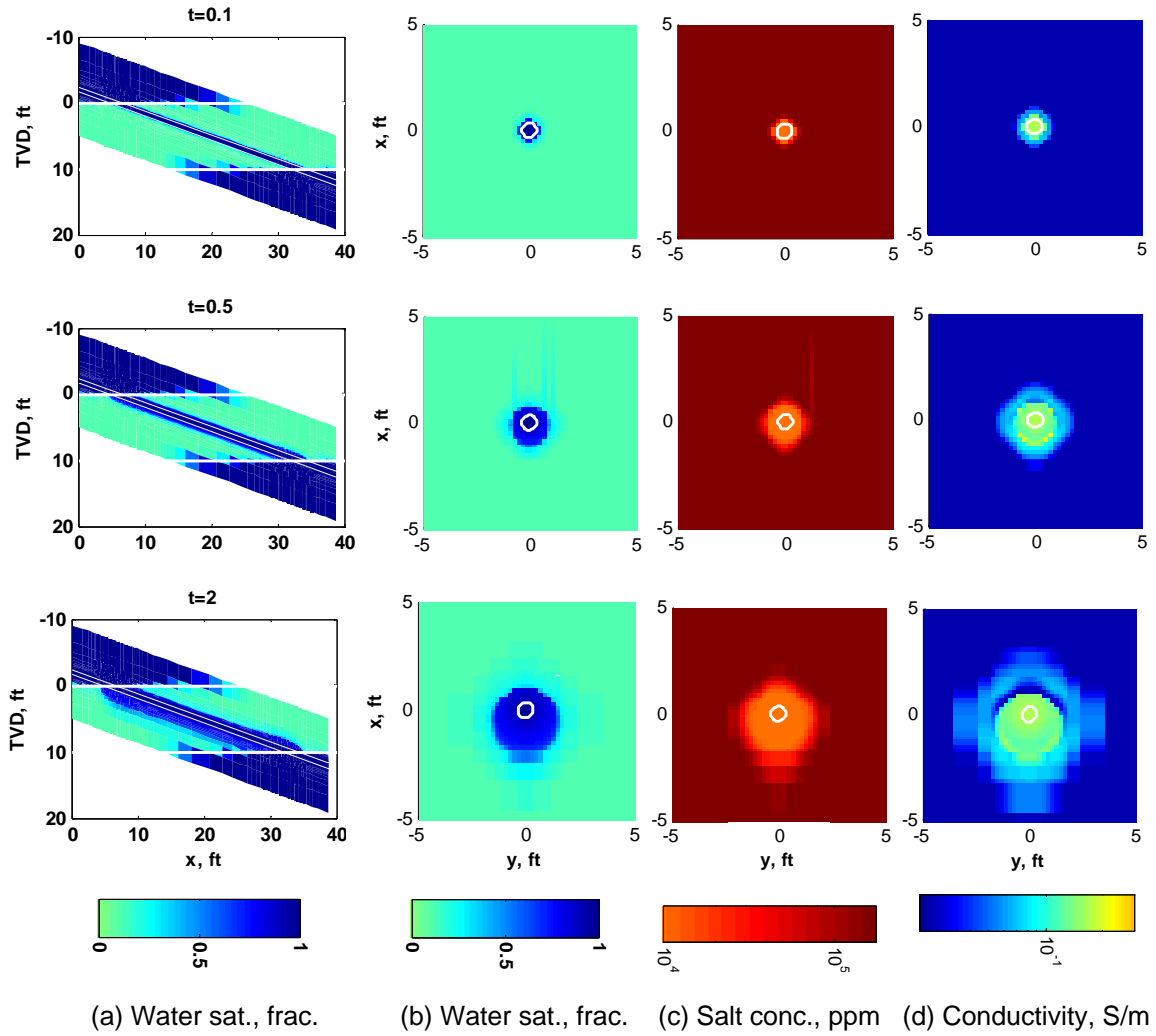


**Figure 2.5:** Spatial distributions of water saturation, salt concentration, and electrical resistivity resulting from the simulation of mud-filtrate invasion with WBM. Panel (a) shows the XZ cross-section of water saturation in the 10-ft layer. Panels (b), (c), and (d) show cross-sections of water saturation, salt concentration, and electrical conductivity, respectively, perpendicular to the borehole axis simulated in the center of the top layer. The first, second, and third rows correspond to  $t=0.1$ ,  $t=0.5$ , and  $t=2$  days of invasion, respectively. Relative dip is  $70^\circ$ .

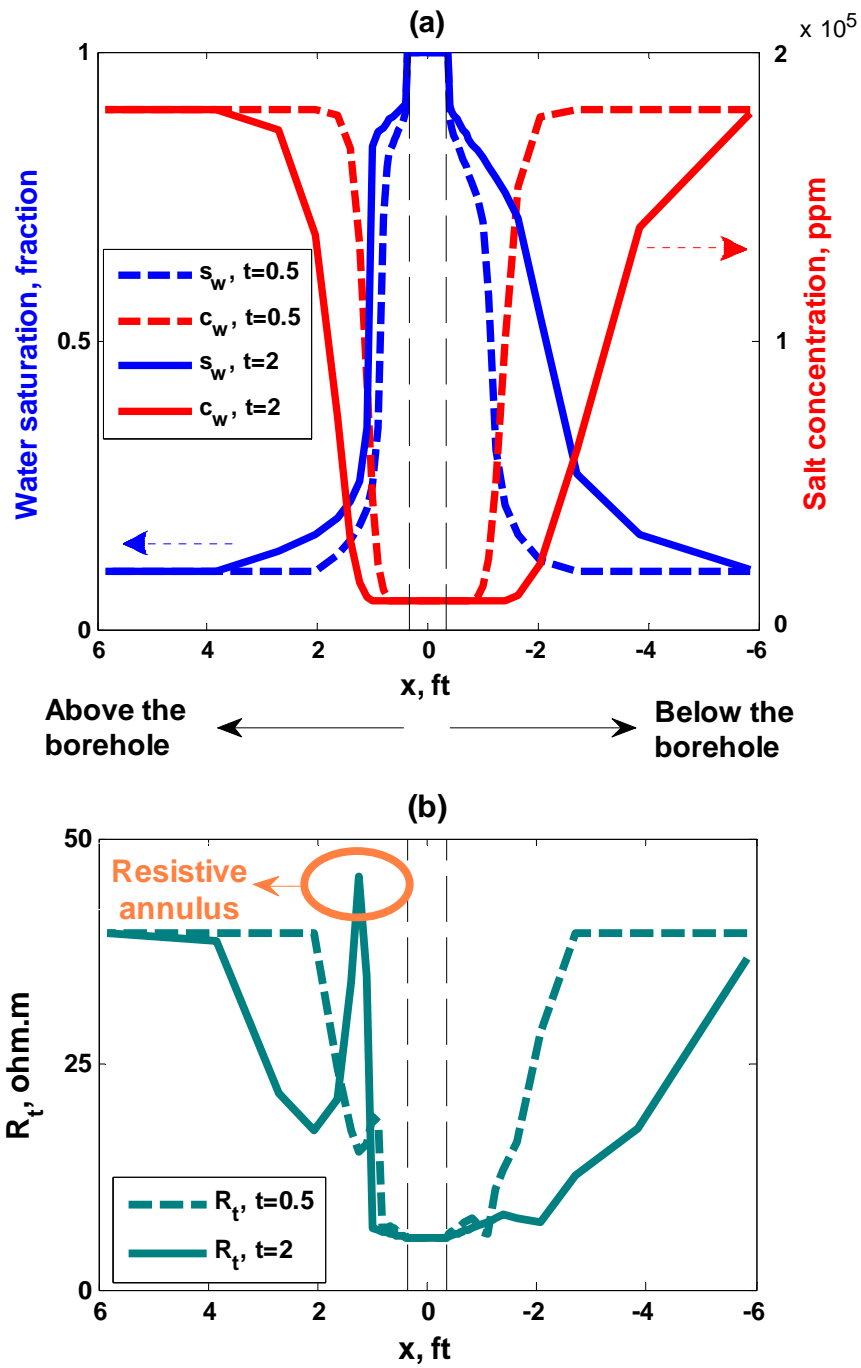


**Figure 2.6:** Radial distributions of (a) water saturation and salt concentration, and (b) formation resistivity, simulated at  $t=0.5$  and  $t=2$  days of WBM-filtrate invasion.

## 2.4 DISCUSSION

Simulations of WBM invasion predicted that a resistive annulus could appear above the borehole in cases of invasion in high-angle wells, while no annulus was present in a vertical well. Because all the assumed petrophysical parameters were identical in the two cases, we remark that the effects of gravity segregation are significant in the spatial distribution of electrical conductivity around highly-deviated wells. As time progresses, simulations indicate that the resistive annulus grows above the borehole. However, the resistive annulus is not observed in all cases. Alpak et al. (2003) described a simulation case study for a horizontal well where they showed a conductive annulus below the borehole due to a water saturation front leading the salt concentration front. The appearance of conductive or resistive annuli in the spatial distribution of electrical conductivity due to WBM invasion is mainly a function of salt concentration contrast between formation connate water and mud filtrate, porosity, absolute and relative permeability, and capillary pressure, among other petrophysical parameters. However, in all cases in which WBM is denser than formation hydrocarbon, we expect a more conductive region below the borehole compared to that above the borehole, owing to unstable displacement and downward segregation of conductive water-base mud in highly deviated wells. This is an important consideration in the interpretation of multi-component induction measurements acquired in high-angle wells because the corresponding effect could be confused with intrinsic electrical anisotropy, for instance.

## **CHAPTER 3**

### **SIMULATION OF MULTI-COMPONENT INDUCTION**

#### **MEASUREMENTS**

This chapter gives details about the numerical simulation of multi-component induction measurements, describing the pseudo electrical anisotropy originating from mud-filtrate invasion. We also consider time-lapse variations of multi-component induction measurements. Lastly, we compare the impact of water-base mud-filtrate invasion on multi-component induction measurements acquired at different angles of wellbore deviation.

#### **3.1 METHOD**

Multi-component induction measurements are simulated with a finite-difference code based on a coupled vector-scalar potential formulation (Hou et al., 2006). In this code, a Cartesian grid is constructed around the tool with the axis of the borehole in the Z-direction and perpendicular to the XY-plane. Multi-component induction measurements are simulated for two sets of transmitter-receiver spacing. We assume a short transmitter-receiver spacing (offset) of 0.4 m and a long spacing of 1.8 m. These transmitter-receiver offsets are consistent with current commercial technologies (Barber et al. 2004). Borehole effects on multi-component induction measurements can be significant. In order to simulate borehole-corrected measurements, we set the borehole conductivity equal to the formation conductivity at the wellbore interface.

### **3.2 APPARENT CONDUCTIVITY**

Multi-component EM simulations generate a  $3 \times 3$  magnetic field matrix at each depth of measurement. We express the calculated magnetic fields in the form of apparent conductivity. There are analytical solutions to transform direct-coupled components of magnetic field into apparent conductivity assuming an infinite homogenous medium (Ward and Hohmann, 1988). For the case of direct-coupled components, we transform the corresponding magnetic fields into apparent conductivity using iterative minimization. We also apply the approximations used by Mallan and Torres-Verdín (2006) to calculate cross-coupled apparent conductivities at each depth of measurement.

### **3.3 SIMULATION RESULTS**

Multi-component logging measurements are simulated for the model shown in Figure 2.1 before and after invasion. Figures 3.1 and 3.2 show the simulated logs acquired in the vertical and  $70^\circ$  wells, respectively. Receiver offset is 0.4 m (short offset) and operating frequency is 25 kHz. Simulation results are shown in the form of apparent conductivity for the direct-coupled (XX, YY, ZZ) and the cross-coupled (XZ, ZX) components. We assumed that the tool azimuth is zero whereby the model becomes symmetric in the Y-direction. Consequently, y-directed cross-coupled (XY, YX, YZ, ZY) components are null and are not included in the figures. For the case of a vertical well, we show only ZZ- and XX-components because the YY-component is identical to the XX-component and the XZ- and ZX-components are null due to symmetry in the X-direction. Simulations of multi-component measurements are repeated with the long transmitter- receiver offset (1.8 m offset). Figure 3.3 shows the apparent conductivity

logs simulated with the long offset. We remark that the long transmitter-receiver offset exhibits a greater volume of investigation than that of the short offset; hence a larger volume of the model is averaged by the measurement.

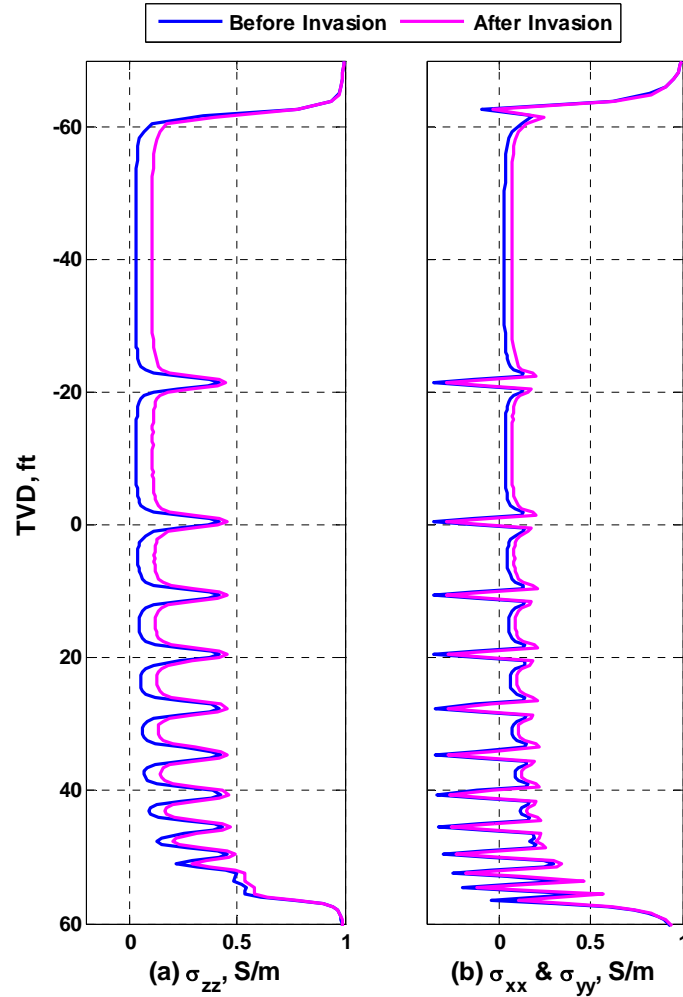


**Figure 3.1:** Comparison of (a)  $\sigma_{zz}$  and (b)  $\sigma_{xx}$  responses simulated before and after 2 days of WBM-filtrate invasion. Receiver offset is 0.4 m and operating frequency is 25 kHz. The well is vertical.

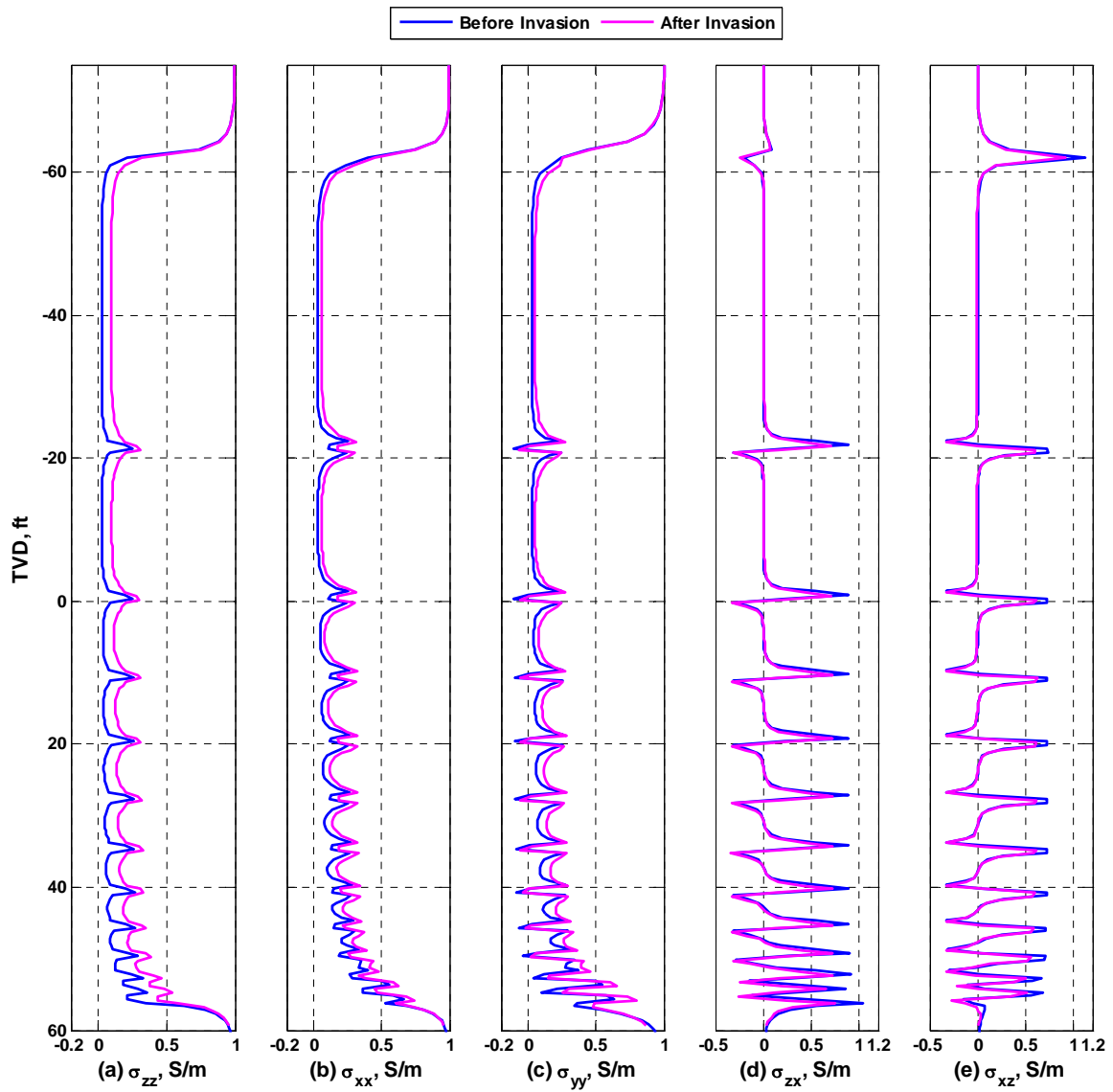


**Figure 3.2:** Comparison of (a)  $\sigma_{zz}$ , (b)  $\sigma_{xx}$ , (c)  $\sigma_{yy}$ , (d)  $\sigma_{zx}$ , and (e)  $\sigma_{xz}$  responses simulated before and after 2 days of WBM-filtrate invasion. Receiver offset is 0.4 m and operating frequency is 25 kHz. Dip angle is  $70^\circ$ .

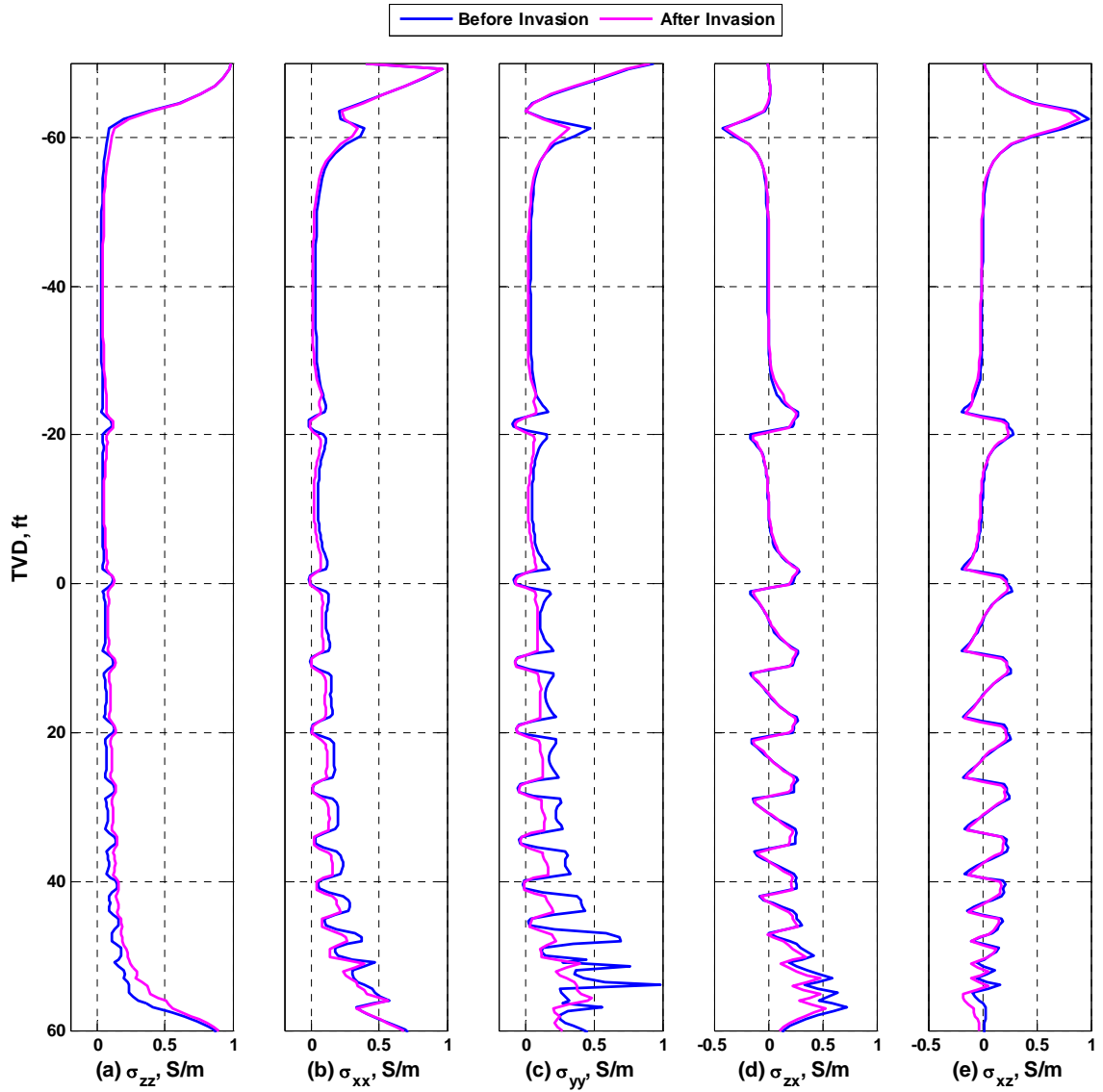


**Figure 3.3:** Comparison of (a)  $\sigma_{zz}$ , (b)  $\sigma_{xx}$ , (c)  $\sigma_{yy}$ , (d)  $\sigma_{zx}$ , and (e)  $\sigma_{xz}$  responses simulated before and after 2 days of WBM-filtrate invasion. Receiver offset is 1.8 m and operating frequency is 25 kHz. Dip angle is  $70^\circ$ .

Simulations show that the transverse components (XX, YY) develops a more complex behavior than the conventional ZZ-response and exhibit strong “horns” at bed boundaries. These characteristic horns are caused by accumulation of electrical charge at bed boundaries. Abnormal horns simulated for the case of long offset are smaller in amplitude than the horns simulated in similar logs for the case of short offset owing to a greater volume of investigation. Furthermore, cross-coupled (XZ and ZX) components are not identical at bed boundaries, thereby indicating a non-symmetric matrix of measurements at bed boundaries even before invasion. Simulations also indicate that WBM invasion uniformly shifts the ZZ-response to an increased apparent conductivity while the XX and YY-components are affected in a different way depending on both transmitter-receiver spacing and time of logging. In the subsections below, we focus the analysis to simulated logs at the top layer (40-ft thick layer) to investigate the pseudo electrical anisotropy originating from mud-filtrate invasion.

### **3.4 PSEUDO ELECTRICAL ANISOTROPY**

In this section we focus the study to the top layer which is the thickest layer in the synthetic multi-layer model. We choose this layer for analysis in order to minimize shoulder-bed effects on multi-component measurements simulated at the center of the layer. Figure 3.4a shows the direct-coupled apparent conductivity logs before invasion for both vertical and 70° wells. All the simulated components yield the true conductivity of the sand unit in the center of the bed where there is no appreciable bed-boundary effect. Consequently, measurements simulated before invasion indicate that the sand layer is isotropic. However, Figure 3.4b indicates a distinction between the

simulated well logs after 2 days of invasion. Transverse (XX, YY) components are still identical for the vertical well since the spatial distribution of invasion around the wellbore is symmetric. By contrast, the difference between transverse components for the case of the 70° well originates from non-symmetric invasion around the borehole. Pseudo electrical anisotropy can be inferred from the differences between transverse components after invasion.

Cross-coupled components are still null after invasion for the vertical well due to spatially symmetric invasion around the borehole. Figure 3.5 compares XZ and ZX apparent conductivity logs before and after invasion simulated in the 70° well. Non-zero XZ and ZX apparent conductivities in the center of the layer are another consequence of non-symmetric invasion, whereby we no longer observe a diagonal matrix of measurements in the center of the layer after invasion. Therefore, in addition to significant changes in diagonal entries, two off-diagonal entries appear in the matrix of measurements after invasion. This matrix structure also arises in the presence of intrinsic anisotropy. The important remark about Figure 3.5 is the opposite sign of the XZ and ZX components. We suggest that this property can be helpful in distinguishing intrinsic anisotropy due to thin laminations from pseudo electrical anisotropy originating from mud-filtrate invasion. The matrix of measurements is symmetric in intrinsically anisotropic thick reservoirs. That is, the XZ and ZX entries are identical. Therefore, the matrix of measurements can be converted to a diagonal matrix by a simple rotation in order to determine vertical and horizontal resistivities. However, in the presence of mud-filtrate invasion, the XZ and ZX components have opposite signs and different

magnitudes. Thus, the matrix of measurements is no longer symmetric and therefore cannot be diagonalized. For instance, the matrix of apparent conductivities in the center of the top layer is given by

$$\sigma = \begin{bmatrix} 0.0256 & 0 & 0 \\ 0 & 0.0256 & 0 \\ 0 & 0 & 0.0256 \end{bmatrix}$$

before invasion for both vertical and 70° wells. After 2 days of invasion the matrix changes to

$$\sigma = \begin{bmatrix} 0.0612 & 0 & 0 \\ 0 & 0.0612 & 0 \\ 0 & 0 & 0.1016 \end{bmatrix},$$

and

$$\sigma = \begin{bmatrix} 0.0551 & 0 & -0.0078 \\ 0 & 0.0504 & 0 \\ 0.0071 & 0 & 0.0972 \end{bmatrix}$$

for the vertical and 70° wells, respectively. This exercise emphasizes that one should never invert the matrix of measurements to infer vertical and horizontal resistivities when multi-component induction measurements are affected by mud-filtrate invasion. Otherwise, inversion will result in false interpretations of electrical anisotropy, i.e. pseudo electrical anisotropy.

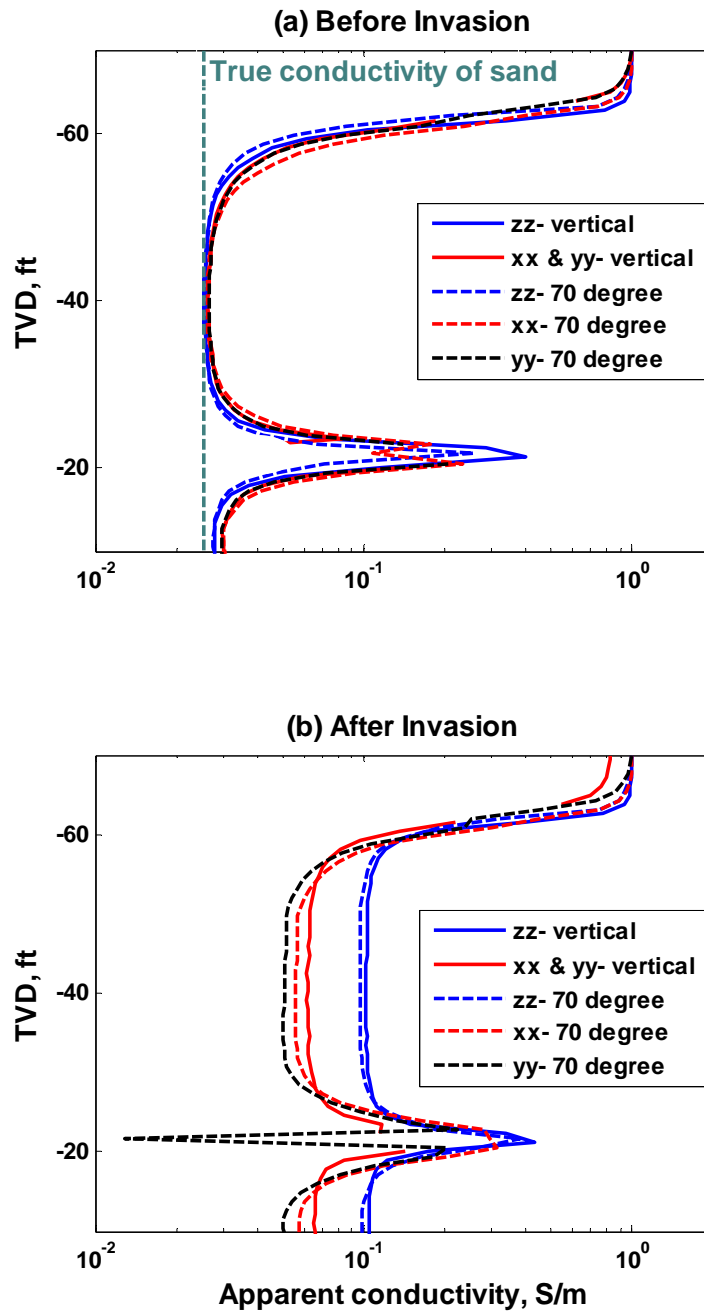


**Figure 3.4:** Direct-coupled components of apparent conductivity (XX, YY, and ZZ) simulated in both vertical and  $70^\circ$  wells (a) before WBM-filtrate invasion, and (b) after 2 days of invasion. Receiver offset is 0.4 m and operating frequency is 25 kHz.

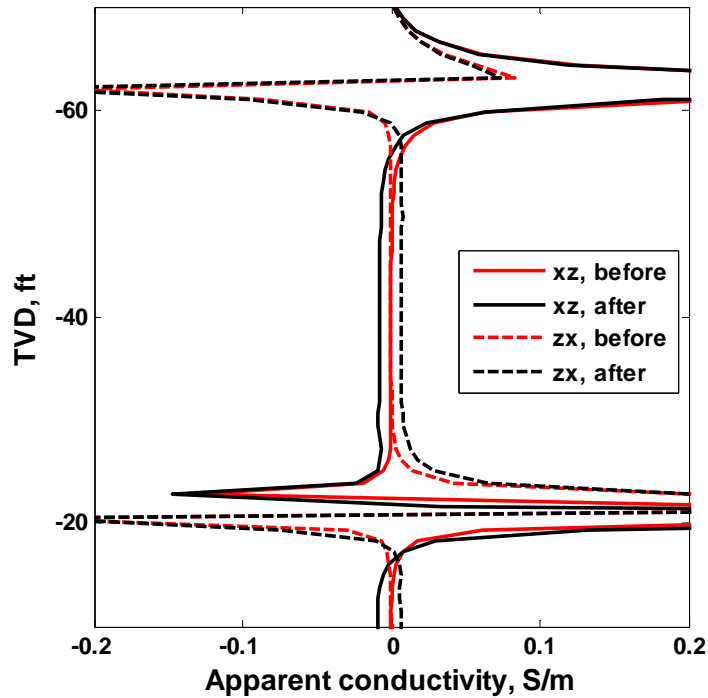


**Figure 3.5:** Cross-coupled components of apparent conductivity (XZ, ZX) simulated in the 70° well compared before and after 2 days of WBM-filtrate invasion. Receiver offset is 0.4 m and operating frequency is 25 kHz.

Whole-space multi-component spatial sensitivity volumes are of great help in understanding multi-component EM measurements (Alumbaugh and Wilt, 2001; Tompkins et al. 2004; Barber et al. 2004). Although these sensitivity functions change significantly in the presence of shoulder beds, dip angle, borehole, and invasion, they shed valuable insight to the interpretation of multi-component responses. The afore-described behavior of the XZ- and ZX-components can be explained with the non-symmetric spatial sensitivity functions associated with them. First, one can infer that symmetric invasion results in null cross-coupled components whereas non-symmetric

invasion leads to non-zero XZ and ZX responses. Second, as conductive mud advances more rapidly further into one side of the borehole due to gravity segregation, the contribution to measurement sensitivity of that spatial region becomes dominant. Therefore, the opposite sign exhibited by the XZ and ZX components arises because their spatial sensitivity volumes are asymmetric.

### **3.5 TIME-LAPSE VARIATION OF MULTI-COMPONENT INDUCTION MEASUREMENTS**

We still focus the description to the simulated logs in the top layer and compare them at different times of acquisition after the onset of invasion. Figure 3.6 shows the direct-coupled (XX, YY, ZZ) and cross-coupled (XZ) responses simulated with the 0.4 m offset (short offset) at different times of invasion. The figure indicates that co-axial apparent conductivity increases monotonically over time. The sensitivity volume associated with the ZZ-component has a positive contribution and, therefore, the ZZ-apparent conductivity log shifts to the right as the conductive WBM advances through the sensitivity region over time. By contrast to the co-axial log, transverse (XX, YY) components initially decrease and subsequently increase with time of invasion. This behavior can also be explained with the corresponding spatial sensitivity functions (Barber et al. 2004). At short times after the onset of invasion, conductive mud occupies mainly the negative sensitivity region around the borehole whereupon the apparent conductivity primarily decreases. As time progresses, the invasion front advances through the negative volume and enters the positive volume, thereby causing an increase of the transverse responses. We suggest that this time-lapse feature of transverse logs can be very helpful in distinguishing invasion effects from other 3D effects, where the non-

monotonic variations of transverse components provide good sensitivity to time-lapse mud-filtrate invasion. Figure 3.6d shows that the ZX-apparent conductivity simulated at the center of the layer increases monotonically over time as the spatial distribution of invasion becomes more spatially asymmetric.

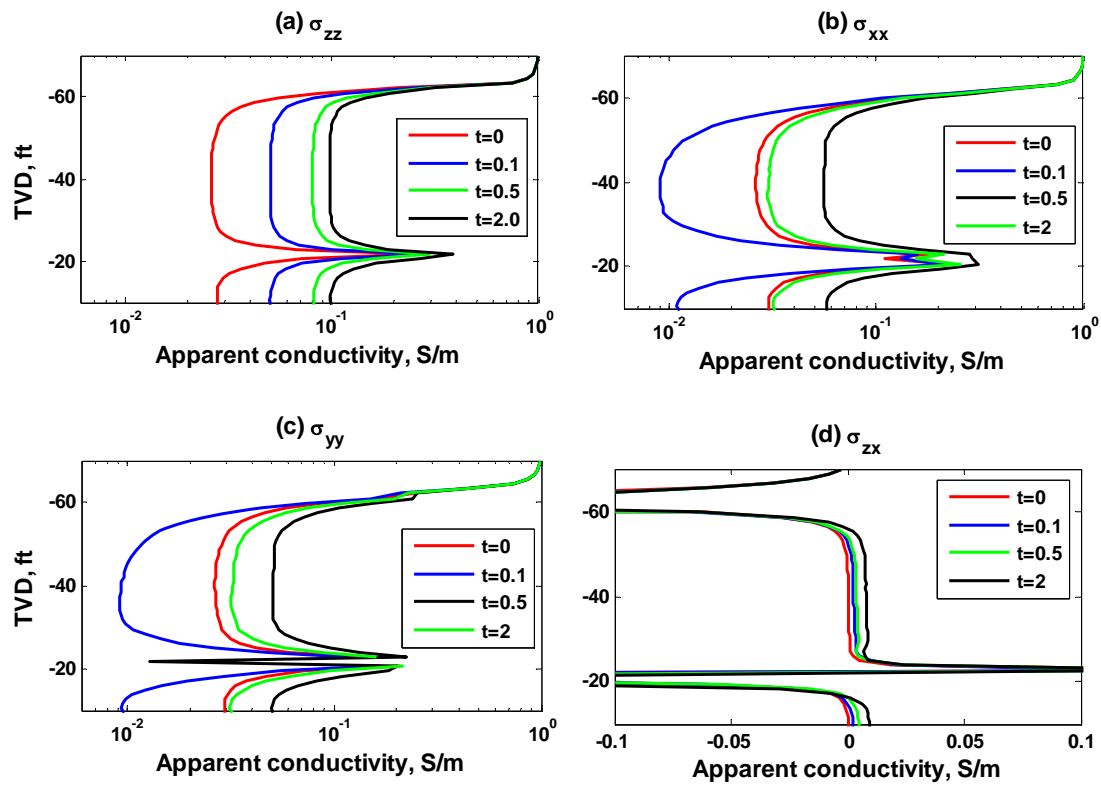


**Figure 3.6:** Comparison of (a)  $\sigma_{zz}$ , (b)  $\sigma_{xx}$ , (c)  $\sigma_{yy}$ , and (d)  $\sigma_{zx}$  responses simulated at different times of acquisition after the onset of WBM-filtrate invasion. Receiver offset is 0.4 m and operating frequency is 25 kHz. Dip angle is  $70^\circ$ .

Figure 3.7 shows the time-lapse variations of transverse components simulated with the 1.8 m transmitter-receiver offset (long offset). Interestingly, transverse components decrease monotonically up to 2 days of invasion. Again, this behavior can be explained by the corresponding spatial sensitivity functions. For the long offset, the negative sensitivity region of transverse components extends further away from the borehole than the one associated with the short offset. Consequently, as time progresses, conductive mud advances further through the negative region and does not enter the positive sensitivity region.

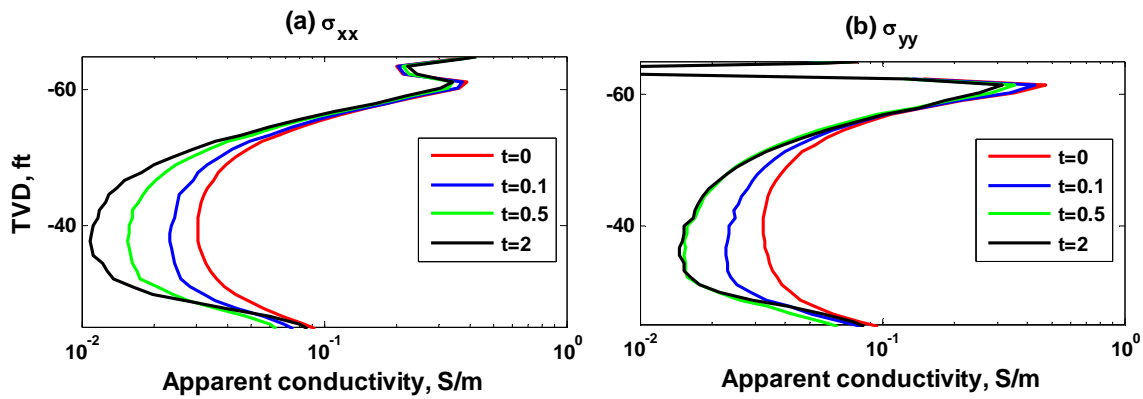


**Figure 3.7:** Comparison of (a)  $\sigma_{xx}$  and (b)  $\sigma_{yy}$  responses simulated at different times of acquisition after the onset of WBM-filtrate invasion. Receiver offset is 1.8 m and operating frequency is 25 kHz. Dip angle is  $70^\circ$ .

Using the approximations proposed by Zhdanov et al. (2001), we calculate apparent vertical and horizontal conductivities at the center of the top layer to confirm time-lapse pseudo electrical anisotropy caused by WBM-filtrate invasion. Tables 3.1 and 3.2 summarize the apparent vertical and horizontal conductivities calculated at different

times of acquisition after the onset of invasion for the vertical and 70° wells, respectively. The approximations correctly indicate that the sand layer is isotropic for both vertical and deviated wells before invasion. However, as the time of invasion increases the calculated values of apparent vertical and horizontal conductivity become different, hence diagnosing pseudo electrical anisotropy originating from mud-filtrate invasion.

Times (days)	$\sigma_h$ (S/m)	$\sigma_v$ (S/m)	Anisotropy ratio
0.0	0.0256	0.0256	1.0
0.1	0.0442	0.0117	3.78
0.5	0.0706	0.0235	3.00
2.0	0.1016	0.0612	1.66

**TABLE 3.1:** Apparent horizontal and vertical conductivities simulated at different times after the onset of invasion in the vertical well.

Times (days)	$\sigma_h$ (S/m)	$\sigma_v$ (S/m)	Anisotropy ratio
0.0	0.0256	0.0256	1.0
0.1	0.0491	0.0090	5.44
0.5	0.0783	0.0301	2.60
2.0	0.0949	0.0508	1.87

**TABLE 3.2:** Apparent horizontal and vertical conductivities simulated at different times after the onset of invasion in the 70° well.

### **3.6 LAYER-THICKNESS EFFECTS**

In this section, we consider the complete model to examine the effects of bed boundary on multi- component induction measurements and compare them to the effects of mud-filtrate invasion. Figure 3.8 shows the deviation of direct-coupled components of apparent conductivity simulated at the center of different sand layers from the true conductivity of sand as a function of layer thickness. We infer that thick layers are much less affected by bed boundary effects than thin layers. However, mud-filtrate invasion affects the measurements regardless of layer thickness. Therefore, deviation of apparent conductivity from the true value of layer conductivity is mainly caused by mud-filtrate invasion in thicker layers while shoulder-bed effects become dominant in thin layers. Figure 3.8 also indicates that co-planar ( $XX$ ,  $YY$ ) components are more affected by both shoulder-bed and invasion effects than the co-axial ( $ZZ$ ) component.

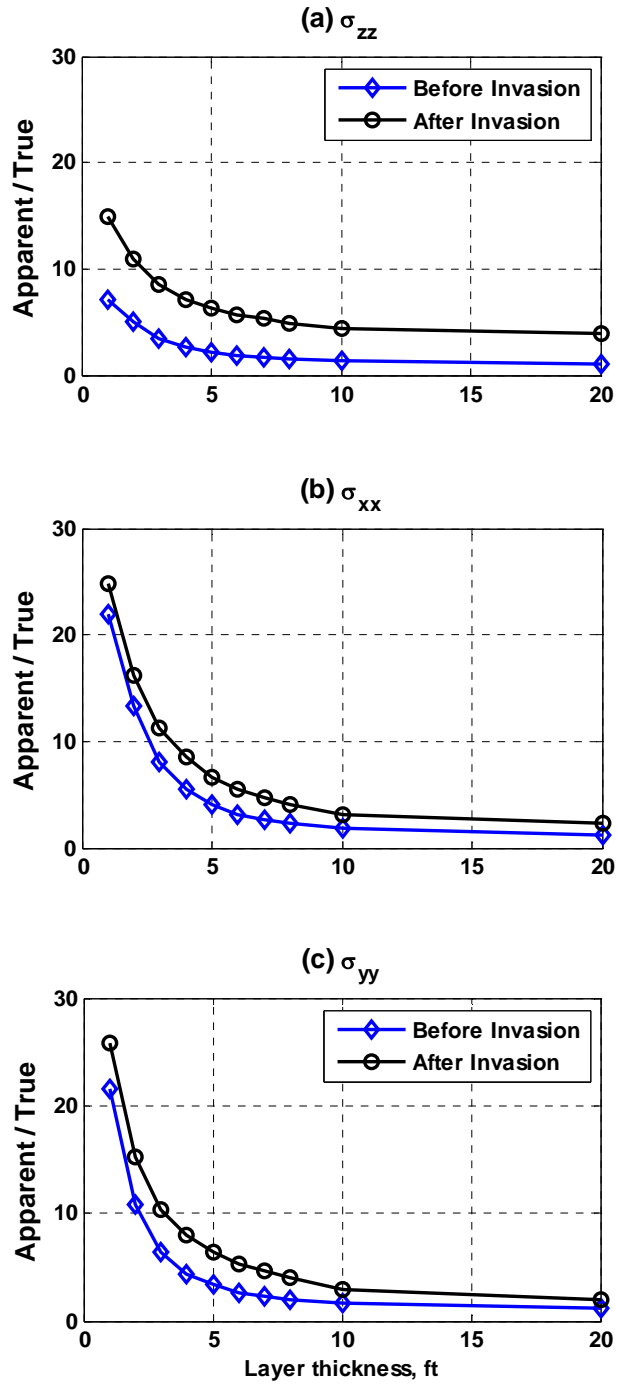


**Figure 3.8:** Deviation of (a)  $\sigma_{zz}$ , (b)  $\sigma_{xx}$ , and (c)  $\sigma_{yy}$ , responses from true layer conductivity simulated in the center of different layers as a function of their thicknesses before and after 2 days of WBM-filtrate invasion.

### 3.7 EFFECT OF WELL-DEVIATION ANGLE

In this section, we compare the impact of water-base mud-filtrate invasion on multi-component induction measurements acquired at different angles of wellbore deviation. Figure 3.9 compares the simulated logs in the vertical, 60°, 70°, and 80° wells after 2 days of WBM invasion. Measurements are very close for 60°, 70°, and 80° wells, especially in the sand layer intervals. Figure 3.10 shows the results at the top layer for the

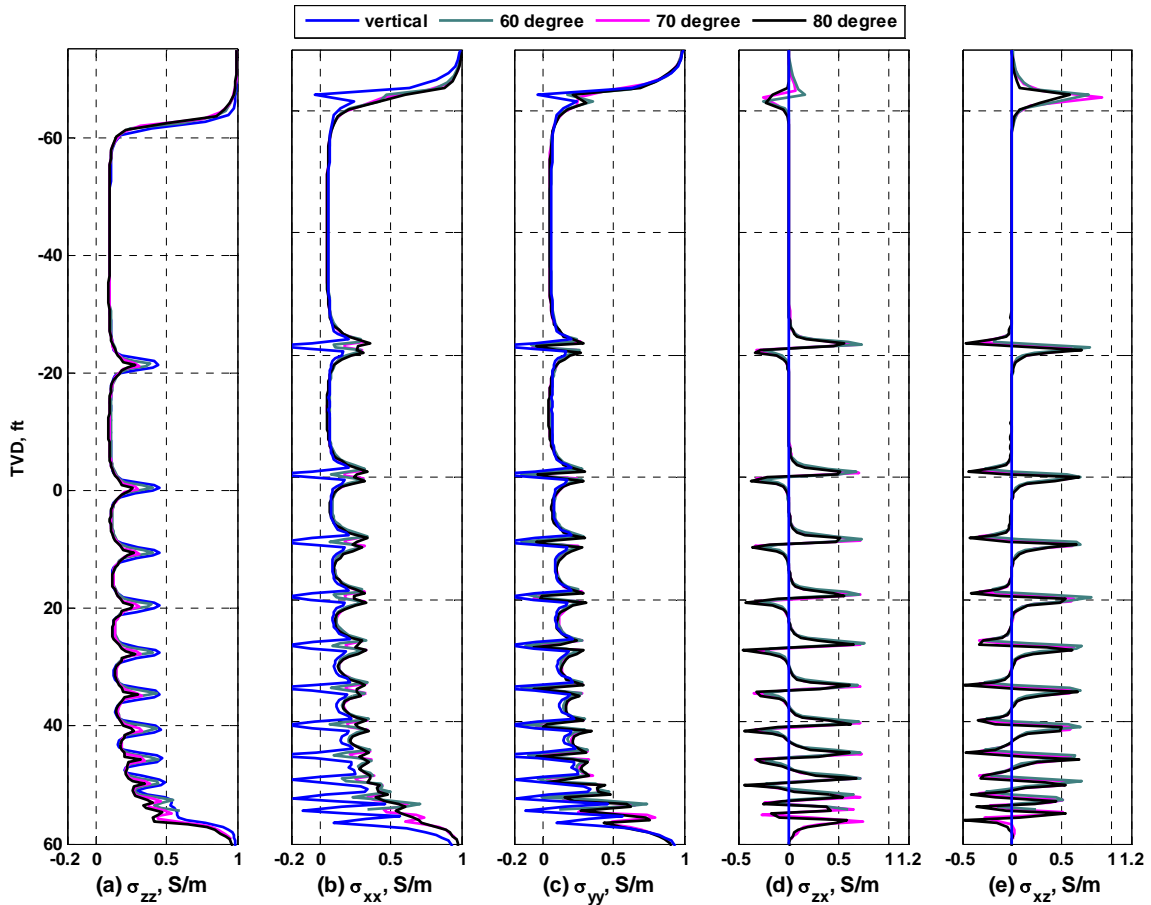


**Figure 3.9:** Comparison of (a)  $\sigma_{zz}$ , (b)  $\sigma_{xx}$ , (c)  $\sigma_{yy}$ , (d)  $\sigma_{zx}$ , and (e)  $\sigma_{xz}$  responses after 2 days of WBM-filtrate invasion simulated for different angles of well deviation. Receiver offset is 0.4 m and operating frequency is 25 kHz.

ZZ and ZX components to emphasize the small differences observed at different angles of wellbore deviation. Figure 3.10b shows that the ZX response in the center of the layer increases as dip angle increases.

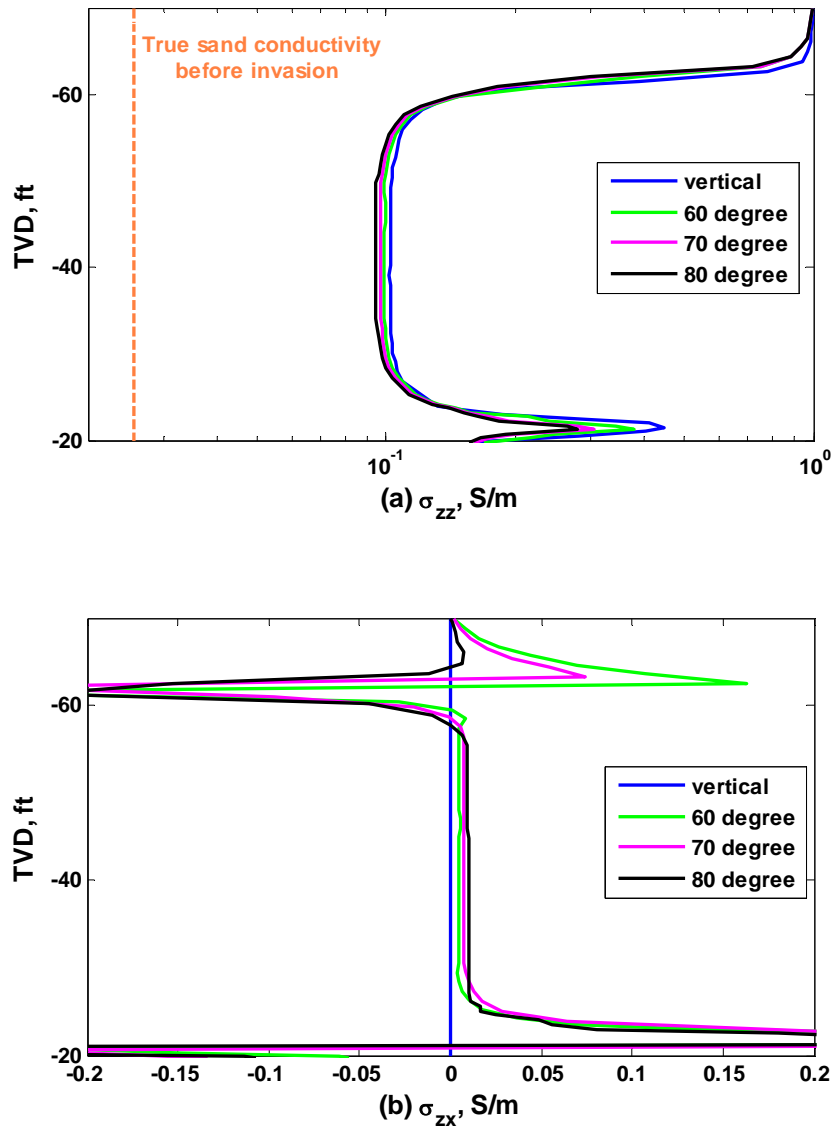


**Figure 3.10:** Comparison of (a)  $\sigma_{zz}$  and (b)  $\sigma_{zx}$  responses at the top layer after 2 days of WBM-filtrate invasion simulated for different angles of well deviation. Receiver offset is 0.4 m and operating frequency is 25 kHz.

## CHAPTER 4

### OIL-BASE MUD-FILTRATE INVASION

This chapter describes the formation model considered for the simulation of oil-base mud-filtrate invasion. Subsequently, we describe the spatial distributions of water saturation and electrical conductivity resulting from the simulation of oil-base mud-filtrate invasion. We also compare multi-component induction measurements simulated before and after oil-base mud-filtrate invasion.

#### 4.1 RESERVOIR MODEL

We use the same numerical method to simulate the process of oil-base mud-filtrate invasion in the synthetic model shown in Figure 2.1. Because of null changes of water saturation and salt concentration after invasion with OBM, multi-component induction measurements remain largely unchanged in the permeable sand layers saturated with oil up to the level of irreducible water saturation,. Therefore, we change the capillary pressure curve assumed in the model while all other petrophysical parameters and fluid properties remain identical to those of the WBM case. Figure 4.1a shows the capillary pressure curve assumed in the simulation of OBM invasion. Figure 4.1b displays the corresponding saturation-height plot emphasizing the top and bottom limits of the reservoir. Table 4.1 summarizes the properties of pseudo components assumed in the simulation of OBM invasion. Invasion rate is 0.4 bbl /day /ft.

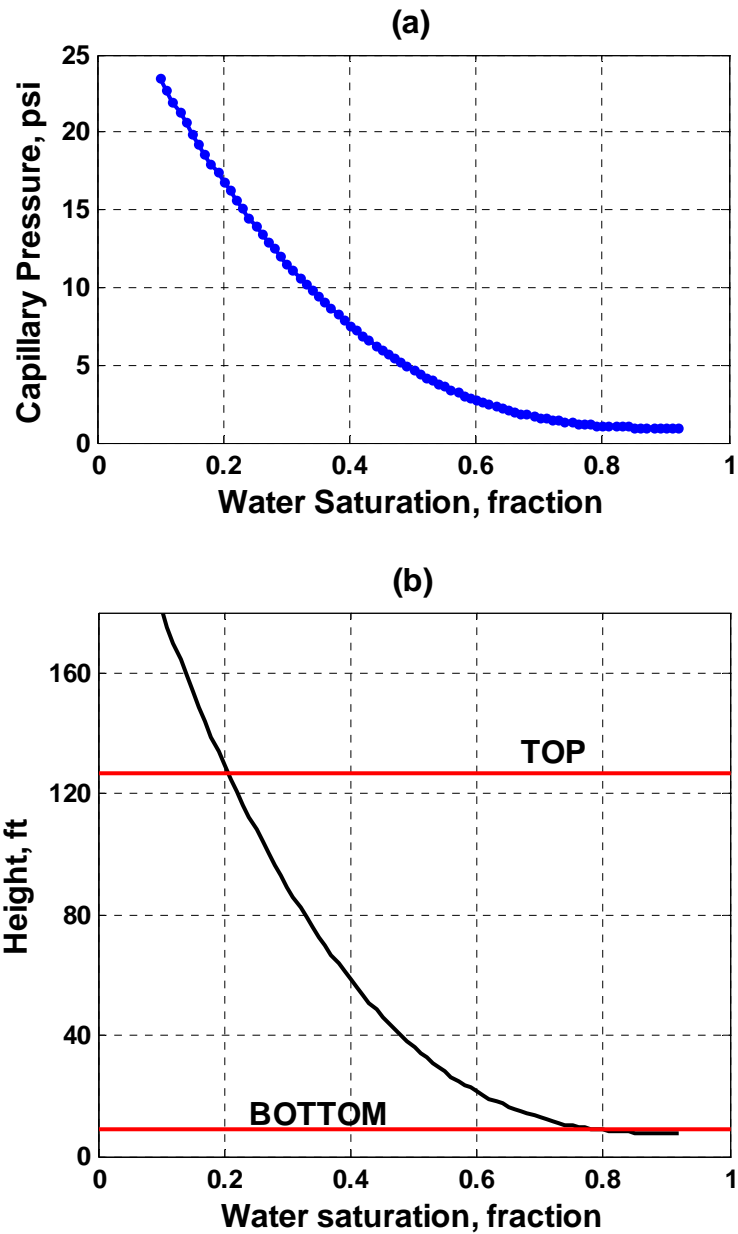


**Figure 4.1:** (a) Wetting-phase saturation-dependent capillary pressure assumed in the simulation of OBM-filtrate invasion, and (b) Corresponding saturation-height distribution showing the top and the bottom limits of the reservoir.

Parameter	In situ (C <sub>7</sub> C <sub>18</sub> )	Mud filtrate (MC <sub>16</sub> )
Molar weight (lbs/mol)	132.8	222.0
Density (gr/cm <sup>3</sup> )	0.7	0.67
Critical pressure (psi)	322.2	240.2
Critical temperature (°F)	656.2	822.5
Viscosity (cp)	0.5	0.5

**TABLE 4.1:** Summary of the properties of pseudo components assumed in the simulation of OBM invasion.

#### 4.2 SIMULATION RESULTS OF OBM INVASION

Figure 4.2 shows cross-sections of the simulated spatial distributions of water saturation and electrical conductivity perpendicular to the borehole axis after 0.1 days of OBM-filtrate invasion. By contrast to the case of WBM, gravity segregation causes mud-filtrate to sag upward around the borehole. These cross-sections are calculated in the center of the 4-ft thick layer in the model shown in Figure 2.1. We choose the 4-ft layer to describe the simulations of invasion because thicker layers exhibit smaller changes of fluid saturations after OBM invasion, whereas the thinner layers are significantly affected by shoulder beds. At the top of the capillary transition zone, OBM radially displaces oil but not water. However, as shown in Figure 4.2a, the range of water saturation values is still small compared to the one assumed in the WBM case. Owing to the fact that there is no salt mixing in the process of invasion, electrical conductivity changes monotonically around the borehole in the OBM case. The sharp contrast of electrical conductivity

observed in Figure 4.2b is related to shale shoulder beds with assumed conductivity of 1 S/m.

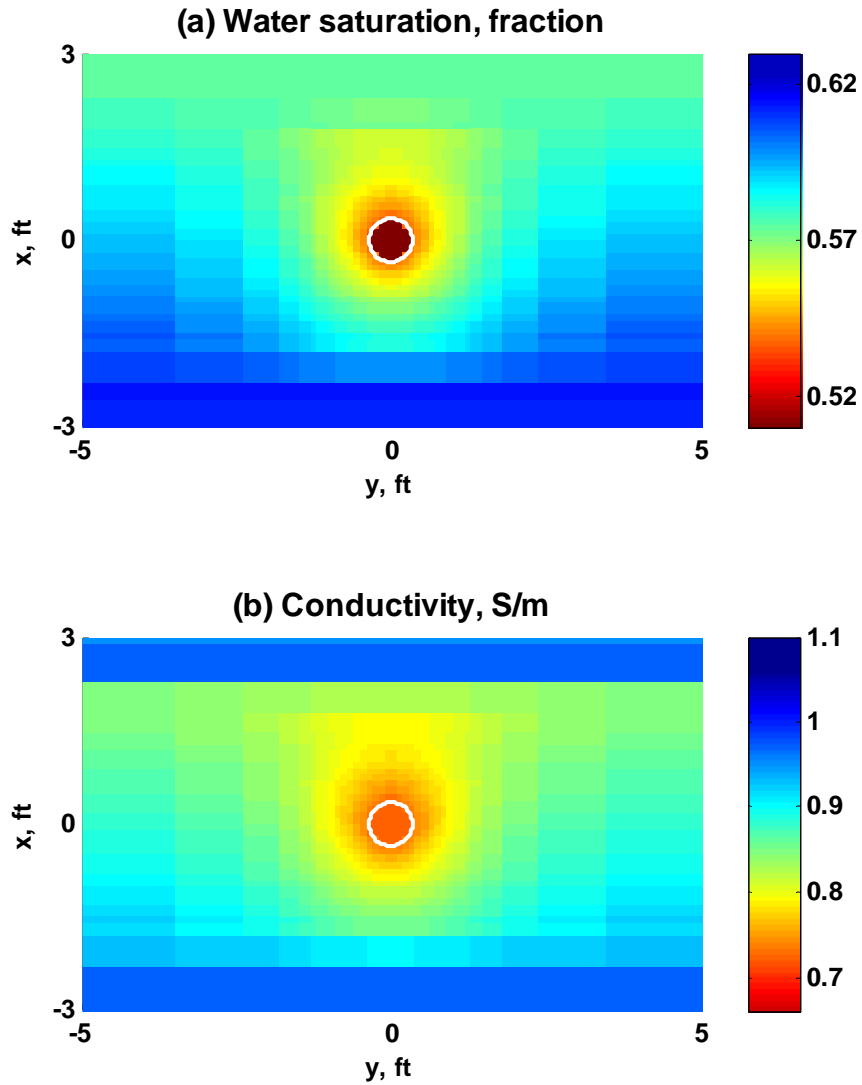


**Figure 4.2:** Cross-sections of the spatial distributions of (a) water saturation, and (b) electrical conductivity, perpendicular to the borehole, simulated after 0.1 days of OBM-filtrate invasion. The images intersect the center of the 4-ft thick layer in the model shown in Figure 2.1. Dip angle is  $70^\circ$ .

### **4.3 SIMULATION OF MULTI-COMPONENT INDUCTION MEASUREMENTS**

Figure 4.3 compares the multi- component induction measurements simulated before and after OBM-filtrate invasion for the case of a  $70^\circ$  well. The simulated responses are not affected by invasion at the top layers where there is a very small change in fluid saturation. However, these effects are pronounced at the thinner layers due to high values of free water saturation before invasion. We conclude that for layers containing less than 40% free water saturation, the effects of OBM-filtrate invasion on multi-component induction measurements are negligible. Figure 4.4 compares the effects of OBM-filtrate invasion on multi-component induction measurements at the bottom of the capillary transition zone for different angles of well deviation. We observe that non-symmetric invasion in highly deviated wells has a greater impact on the simulated measurements than symmetric invasion in the vertical well.

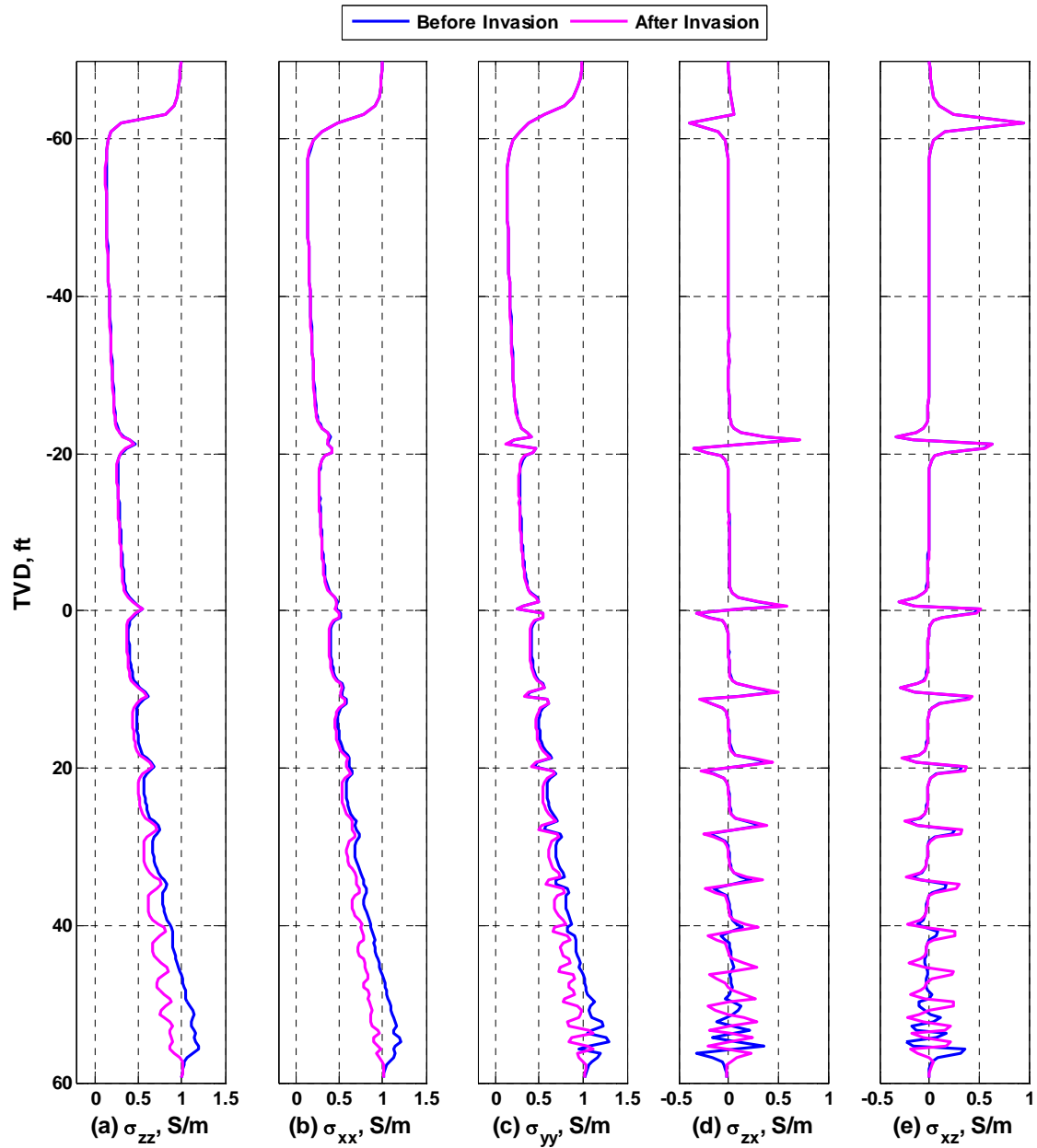


**Figure 4.3:** Comparison of (a)  $\sigma_{zz}$ , (b)  $\sigma_{xx}$ , (c)  $\sigma_{yy}$ , (d)  $\sigma_{zx}$ , and (e)  $\sigma_{xz}$  responses simulated before and after 2 days of OBM-filtrate invasion. Receiver offset is 0.4 m and operating frequency is 25 kHz. Dip angle is  $70^\circ$ .

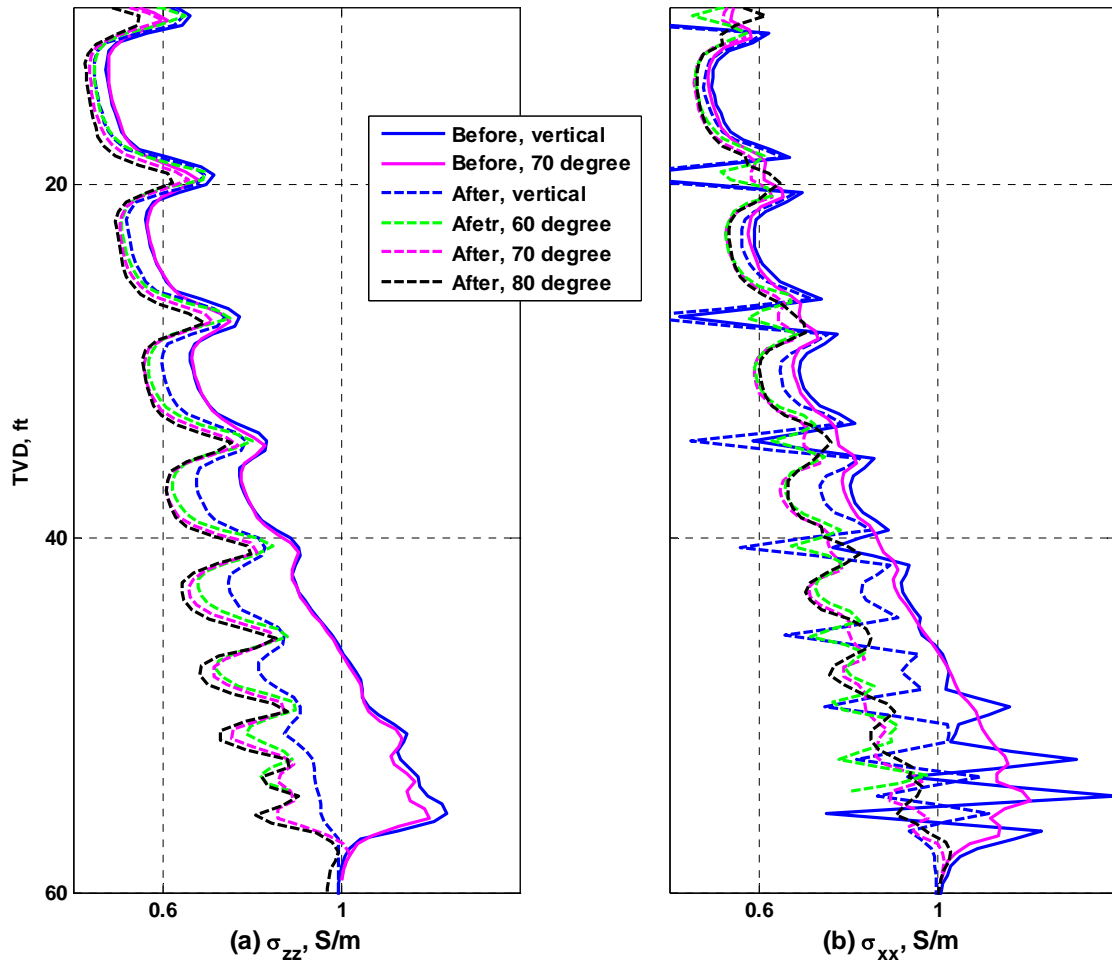


**Figure 4.4:** Comparison of (a)  $\sigma_{zz}$ , and (b)  $\sigma_{xx}$  responses simulated for different angles of well deviation before and after 2 days of OBM-filtrate invasion. Receiver offset is 0.4 m and operating frequency is 25 kHz.

## **CHAPTER 5**

### **SUMMARY AND CONCLUSIONS**

#### **5.1 SUMMARY**

We examined the sensitivities of the various induction components to invasion and time of logging. Time-lapse variations of multi-component induction measurements reflect their sensitivity to the shape and spatial extent of the invasion front. We showed that multi-component induction measurements are affected by both WBM and OBM invasion. However, results from our study indicate that invasion effects for the case of WBM are significantly more important for the reliable interpretation of measurements. On the other hand, our simulations indicate that the effects of OBM-filtrate invasion on multi-component measurements are negligible in hydrocarbon-bearing zones. We also emphasize that mud-filtrate invasion not only gives rise to pseudo electrical anisotropy in isotropic reservoirs, but also significantly affects the electrical anisotropy measured in intrinsically anisotropic reservoirs.

#### **5.2 CONCLUSIONS**

It is important to consider flow behavior accurately to quantify time-lapse effects of mud-filtrate invasion on multi-component induction measurements. Simulations show that gravity segregation in high-angle wells causes water- and oil-base mud-filtrate to sag downward and upward, respectively, around the borehole over time. The resistive

annulus observed above the borehole for the case of WBM invasion in the 70° well is the result of unstable fluid displacement around the borehole. Simulations indicate that the salt concentration front leads the water saturation front above the borehole as time progresses. Furthermore, no-flow boundary conditions at impermeable shale boundaries cause different spatial distributions of electrical conductivity at the top and bottom of sand layers.

Multi-component measurements acquired in the center of the thickest layer (the top layer) indicate that the off-diagonal components ( $XZ$ ,  $ZX$ ) appear in the matrix of measurements with opposite signs after invasion while they are null before invasion. Therefore, by contrast to measurements acquired in an intrinsically anisotropic layer, the matrix of measurements is non-symmetric and therefore is not diagonalizable. Moreover, simulations show that the direct-coupled apparent conductivity logs are no longer aligned in the center of the layer after invasion, indicating pseudo electrical anisotropy originating from mud-filtrate invasion. More importantly, time-lapse variations of multi-component measurements distinguish the effects of mud-filtrate invasion from other 3D effects. Simulations also indicate that co-planar components exhibit non-monotonic changes depending on receiver offset and time of logging. Approximated apparent horizontal and vertical conductivities in the center of the top layer confirm time-lapse pseudo electrical anisotropy due to invasion. Consequently, multi-component induction measurements should never be inverted blindly to compute vertical and horizontal conductivities in the presence of mud-filtrate invasion. Diagnosis and separation of 3D

effects on multi-component induction measurements is necessary prior to inferring electrical anisotropy from the matrix of measurements.

Simulations also show that the effects of oil-base mud-filtrate invasion on multi-component induction measurements are negligible in hydrocarbon-bearing zones containing less than 40% free water.

## REFERENCES

- Alpak, O., Dussan V., E., Habashy, T. and Torres-Verdín, C., 2003, Numerical simulation of mud-filtrate invasion in horizontal wells and sensitivity analysis of array induction tools: *Petrophysics*, vol. 44, no. 6, p. 396-411.
- Alumbaugh, D., and Wilt, M., 2001, A numerical sensitivity study of three dimensional imaging from a single borehole: *Petrophysics*, vol. 42, no. 1, p. 19–31.
- Angeles, R., 2009, Simulation and interpretation of formation-tester measurements acquired in the presence of mud-filtrate invasion, multi-phase flow, and deviated wellbores: Ph.D. Dissertation, The University of Texas at Austin.
- Archie, G. E., 1942, The electrical resistivity log as an aid in determining some reservoir characteristics: *Petroleum Transactions of the AIME*, vol. 146, p. 54–62.
- Barber, T., Anderson, B., Abubakar, A., Broussard, T., Chen, K.C., Davydycheva, S., Druskin, V., Habashy, T., Homan, D., Minerbo, G., Rosthal, R., Schlein, R. and H. Wang, 2004, Determining formation resistivity anisotropy in the presence of invasion: Paper SPE 90526, Society of Petroleum Engineers, presented at Annual Technical Conference and Exhibition, Houston, TX, September 26-29.
- Clavaud, J-B., Nelson, R., Udit Kumar Guru, and Wang, H., 2005, Field example of enhanced hydrocarbon estimation in thinly laminated formation with a tri-axial array induction tool; a laminated sand-shale analysis with anisotropic shale: Paper WW, 46th SPWLA Annual Symposium, New Orleans, LA, June 26-29.
- Gomes, R., Denicol, P., da Cunha, A., de Souza, M., Kriegshauser, B., Payne, C., and Santos, A., 2002, Using multi-component induction log data to enhance formation evaluation in deepwater reservoirs from Campos Basin, offshore Brazil: Paper N, 43rd SPWLA Annual Logging Symposium, Oiso, Japan, June 2-5.
- Hou, J., Mallan, R. K., and Torres-Verdín, C., 2006, Finite-difference simulation of borehole EM measurements in 3D anisotropic media using coupled scalar-vector potentials: *Geophysics*, vol. 71, no. 5, p. G225-G233.
- Klein, J., Martin, P., and Allen, D., 1997, The petrophysics of electrically anisotropic reservoirs: *The Log Analyst*, May-June 1997.
- Kriegshauser, B., Fanini, O., Yu, L., van der Horst, J., and van Popta, J., 2001, Improved shaly sand interpretation in highly deviated and horizontal wells using multi-component induction log data: Paper S, SPWLA 42<sup>nd</sup> Annual Logging Symposium Transaction, Houston, TX, June 17-20.

- Mallan, R. K., and Torres-Verdín, C., 2006, Effects of petrophysical, environmental, and geometrical parameters on multi-component induction measurements acquired in high-angle wells: *Petrophysics*, vol. 48, no. 4, p. 225-241.
- Mollison, R.A., Schoen J., Fanini O., Kriegshauser B., Meyer W.H., and Gupta P.K., 1999, A model for hydrocarbon saturation determination from an orthogonal tensor relationship in thinly laminated, anisotropic reservoirs: Paper OO, 40th SPWLA Annual Logging Symposium, Oslo, Norway, May 30 - June 3.
- Omeragic, D., Dumont, A., Esmersoy, C., Habashy, T., Li, Q., Minerbo, G., Rosthal, R., smits, J., Tabanou, J., Schlumberger Oilfield Services, 2006, Sensitivity of directional electromagnetic measurements for well placement and formation evaluation while drilling: 76th SEG Annual meeting, New Orleans, LA, October.
- Rabinovich, M., and Tabarovsky, L., 2001, Enhanced anisotropy from joint processing of multi-component and multi-arrays induction tools: Paper HH, 42nd SPWLA Annual Logging Symposium, Houston, TX, June 17-20.
- Saxana K., and Klimentos, T., 2004, Field study of integrated formation evaluation in thinly laminated reservoirs: Paper SSS. 45th SPWLA Annual Logging Symposium, Noordwijk, The Netherlands, June 6-9.
- Tompkins, M. J., Alumbaugh, D. L., Stanley, D. T., and Lu, X., 2004, Numerical analysis of near borehole and anisotropic layer effects on the response of multi-component induction logging tools: *Geophysics*, vol. 69, no. 1, p. 140–151.
- Ward S.H., Hohmann, G.W., Electromagnetic Theory for geophysical applications, Chapter 4: *Electromagnetic Methods in Applied Geophysics*, Edited by Nabighian M. N., vol. 1, Society of Exploration Geophysicists, USA, 1988.
- Wu, J., Torres-Verdín, C., Sepehrnoori, K., Delshad, M., 2001, Numerical simulation of mud-filtrate invasion in deviated wells: Paper SPE 71739, Society of Petroleum Engineers, presented at Annual Technical Conference and Exhibition, New Orleans, LA, September 30 – October 2.
- Yu, L., Kriegshauser, B., Fanini, O., and Xiao, J., 2001, A fast inversion method for multi-component induction log data: SEG 71st Annual International Meeting, Expanded Abstracts, San Antonio, TX, September 9-14.
- Zhang, J-H., Hu, Q., and Liu, Z-H., 1999, Estimation of true formation resistivity and water saturation with a time-lapse induction logging method: *The Log Analyst*, vol. 40, no. 2, p. 138-148.
- Zhang, Z., Yu, L., Kriegshauser, B., and Chundururu, R., 2001, Simultaneous determination of relative angles and anisotropic resistivity using multi-component

induction logging data: paper Q, Transactions of the SPWLA 42nd Annual Logging Symposium, Houston, TX, June 17-20.

Zhdanov, M., Kennedy, D., and Peksen, E., 2001, Foundations of tensor induction well-logging: *Petrophysics*, vol. 42, no. 6, p. 588-610.